

Interplay of electronic crystals with integer and fractional Chern insulators in moiré pentalayer graphene

Dacen Waters^{1,2*}, Anna Okounkova^{1*}, Ruiheng Su^{3,4}, Boran Zhou⁵, Jiang Yao¹, Kenji Watanabe⁶, Takashi Taniguchi⁷, Xiaodong Xu^{1,8}, Ya-Hui Zhang⁵, Joshua Folk^{3,4}, and Matthew Yankowitz^{1,8†}

¹*Department of Physics, University of Washington, Seattle, Washington, 98195, USA*

²*Intelligence Community Postdoctoral Research Fellowship Program,*

University of Washington, Seattle, Washington, 98195, USA

³*Quantum Matter Institute, University of British Columbia, Vancouver, British Columbia, V6T 1Z1, Canada*

⁴*Department of Physics and Astronomy, University of British Columbia, Vancouver, British Columbia, V6T 1Z1, Canada*

⁵*Department of Physics and Astronomy, Johns Hopkins University, Baltimore, Maryland, 21205, USA*

⁶*Research Center for Electronic and Optical Materials, National Institute for Materials Science, 1-1 Namiki, Tsukuba 305-0044, Japan*

⁷*Research Center for Materials Nanoarchitectonics, National Institute for Materials Science, 1-1 Namiki, Tsukuba 305-0044, Japan*

⁸*Department of Materials Science and Engineering, University of Washington, Seattle, Washington, 98195, USA*

**These authors contributed equally to this work. and*

†myank@uw.edu (M.Y.)

The rapid development of moiré quantum matter has recently led to the remarkable discovery of the fractional quantum anomalous Hall effect [1–6], and sparked predictions of other novel correlation-driven topological states [7–29]. Here, we investigate the interplay of electronic crystals with integer and fractional Chern insulators in a moiré lattice of rhombohedral pentalayer graphene (RPG) aligned with hexagonal boron nitride. At a doping of one electron per moiré unit cell, we see a correlated insulator with a Chern number that can be tuned between $C = 0$ and $+1$ by an electric displacement field, accompanied by an array of other such insulators formed at fractional band fillings, ν . Collectively, these states likely correspond to trivial and topological electronic crystals, some of which spontaneously break the discrete translational symmetry of the moiré lattice. Upon applying a modest magnetic field, a narrow region forms around $\nu = 2/3$ in which transport measurements imply the emergence of a fractional Chern insulator, along with hints of weaker states at other fractional ν . In the same sample, we also see a unique sequence of incipient Chern insulators arising over a broad range of incommensurate band filling near two holes per moiré unit cell. Our results establish moiré RPG as a fertile platform for studying the competition and potential intertwining of electronic crystallization and topological charge fractionalization.

Moiré materials with flat bands have become ideal platforms for studying the interplay between strongly correlated and topological states of matter [30–34]. Early

work in this field established the existence of a wide range of correlation-driven topological states within the magnetic subbands of the Hofstadter butterfly spectrum, including states that break the translational symmetry of the moiré lattice (called “symmetry-broken Chern insulators”) and others that exhibit fractionalized charge excitations (fractional Chern insulators, FCI) [35, 36]. Recently, remarkable progress has been made in achieving analogous states that appear even in the absence of an external magnetic field in moiré lattices with flat bands and suitable quantum geometry. Prominent examples include the integer and fractional quantum anomalous Hall (IQAH and FQAH) states found in twisted bilayer MoTe₂ [1–4] and moiré lattices of rhombohedral multilayer graphene with aligned hBN [5, 6, 37], as well as correlated Chern insulator states with associated translational symmetry breaking found in a variety of other twisted graphene moiré lattices [38–40].

Forming Chern insulators in moiré lattices requires spontaneous valley polarization, resulting in broken time-reversal symmetry [33, 34]. Many-body gaps can be opened at integer fillings of the moiré flat bands, resulting in the emergence of Chern insulators and the IQAH effect when the filled bands have nonzero total Chern number. Topological gapped states can also form at fractional fillings of the moiré bands, but require the assistance of additional correlation-driven mechanisms. FQAH states are a notable example, forming anyonic quasiparticles but otherwise not needing to break any of the remaining symmetries of the system. Alternatively, electrons can spontaneously break translational symmetry to form topological electronic crystal (TEC) states. Examples include the anomalous Hall crystal (AHC) recently considered for moiré and non-moiré rhombohedral pentalayer graphene

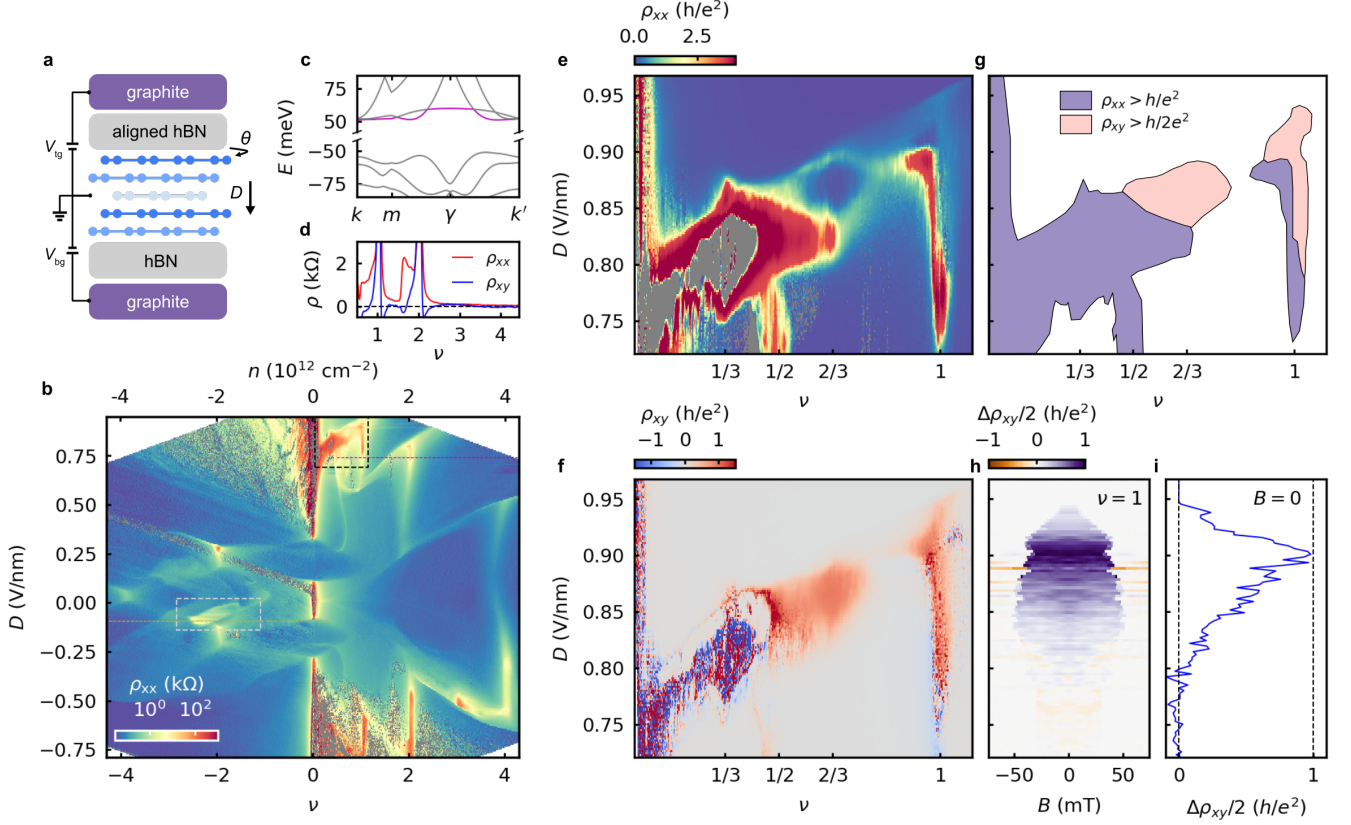


FIG. 1. Device transport characterization and correlated states at $\nu \leq 1$. **a**, Schematic of the device. RPG is encapsulated between flakes of hBN with graphite top and bottom gates. The RPG is misaligned from the bottom hBN, and has a small twist angle of $\theta = 0.90^\circ$ with the top hBN to form a moiré superlattice (see Methods for discussion). **b**, Map of ρ_{xx} taken at $B = 0$ over a wide range of the $n - D$ parameter space. The data is acquired in multiple sub-measurements to mitigate measurement artifacts, as described in the Methods. The dashed black (gray) box indicates the region of data shown in **e-f** (Fig. 4a). The gray colored data in the color scale indicates that ρ_{xx} was measured to be negative, indicating either a highly resistive state or poor equilibration of the contacts (see Methods). **c**, Single-particle calculated band structure with $\delta = +150$ meV and a moiré period of 10.8 nm. This sign of δ corresponds to $D > 0$. The lowest moiré conduction band is colored in purple. **d**, Line traces of ρ_{xx} and ρ_{xy} acquired at $D = 0.740$ V/nm (corresponding to the position of the purple dashed line in **b**) with $B = 0.2$ T (not symmetrized). **e**, Zoomed-in map of ρ_{xx} symmetrized at $|B| = 100$ mT from the region of the black dashed box in **b**. **f**, Similar map of antisymmetrized ρ_{xy} . **g**, Schematic indicating transport features seen in **e-f**. Regions shaded in pink satisfy the condition $\rho_{xy} > h/2e^2$. Regions shaded in purple satisfy the condition $\rho_{xx} > h/e^2$. Regions satisfying both conditions are also shaded in purple (since the large value of ρ_{xy} is an artifact corresponding to mixing with ρ_{xx}). Regions with negative ρ_{xx} are shaded in purple, as they correspond to measurement artifacts in very insulating states (see Methods). **h**, Map of $\Delta\rho_{xy}/2 = (\rho_{xy}^\uparrow - \rho_{xy}^\downarrow)/2$ at $\nu = 1$, where the arrows indicate the direction B is swept. **i**, A line cut of $\Delta\rho_{xy}/2$ from **h** at $B = 0$.

(RPG) [14–16, 18, 21–27], and the generalized AHC seen in twisted bilayer-trilayer graphene [40]. Understanding the interplay between TEC states and FQAH states stands as a critical open challenge for the field.

Here, we study an array of correlation-driven topological states arising in a RPG/hBN moiré lattice with a period of 10.8 nm. Recent pioneering work on this system revealed the emergence of FQAH states at several Jain-sequence fractions for $\nu < 1$, all arising in a device with a slightly larger moiré period of 11.5 nm [5]. In contrast, our device instead exhibits a sequence of trivial insulators and IQAH states, with Chern numbers of $C = 0$ and

$+1$, originating from both integer and fractional fillings of the electron-doped moiré conduction band. These states most likely correspond to trivial ($C = 0$) and topological ($C = +1$) electronic crystals, separated by a phase transition controlled by doping, n , electric displacement field, D , and out-of-plane magnetic field, B . They are most robust near commensurate band fillings ($\nu = 4n/n_s = 1/3, 2/3$, and 1 , where n_s is the moiré superlattice density, see Methods), but nevertheless extend over a wide range of moiré band filling, $0 < \nu \lesssim 1$. Strikingly, there are clear signatures of an incipient FCI state that emerges in a magnetic field of around 2 T and originates from

$\nu = 2/3$, along with hints of other Jain-sequence states. In a different part of the gate-tuned phase diagram, a set of unique topological states form in a distinct valley-polarized pocket near a doping of two holes per moiré unit cell ($\nu \approx -2$). There, we see an incipient Chern insulator emerging from an incommensurate filling of $\nu \approx -2.45$, as well as an unusual sequence of at least 10 weaker topological states arising as the hole doping is reduced. Collectively, our observations pose several intriguing new puzzles for future studies.

Trivial and topological electronic crystals

Figure 1a shows a schematic of our device, in which RPG is nearly aligned to one hBN dielectric but misaligned from the other. The top and bottom graphite gates enable independent control over n and D , the latter of which we define to be positive when electrons are pushed away from the moiré interface. Figure 1b shows a map of the longitudinal resistance, ρ_{xx} , of the device taken over a wide range of n and D . We extract the density needed to fully fill the lowest moiré bands ($\nu = \pm 4$) to be $n_s = 3.98 \times 10^{12} \text{ cm}^{-2}$, corresponding to a moiré period of 10.8 nm and a twist angle between the RPG and hBN of $\theta = 0.90^\circ$ (assuming a 1.7% lattice mismatch between graphene and hBN). Overall, the salient features we see are consistent with those reported in a prior study of moiré RPG [5], including a series of insulating states at the charge neutrality point ($\nu = 0$) and resistive states at various integer values of ν corresponding to correlated or single-particle band insulators. In the Methods section, we provide additional supporting details for all of the descriptions and analysis above (see also Extended Data Figs. 1-2).

Figure 1c shows a continuum model band structure calculation for an interlayer potential difference of $\delta = +150 \text{ meV}$ (see Methods). The calculation predicts that the lowest moiré conduction band (colored in purple) is gapped from the highest moiré valence band, but overlaps the second conduction band. Both of these features are consistent with the experiment, in which there is an insulating state at $\nu = 0$ but a metallic state at $\nu = 4$ for large positive D (see Fig. 1d for a representative measurement at $D = 0.740 \text{ V/nm}$, corresponding to the purple dashed line in Fig. 1b). Figures 1e-f show zoomed-in maps of the field-symmetrized longitudinal (ρ_{xx}) and anti-symmetrized Hall (ρ_{xy}) resistances in the high- D region between $\nu = 0$ and $\nu \approx 1$, outlined by the black dashed square in Fig. 1b. The key features seen in these maps are summarized in Fig. 1g, where regions of $\rho_{xy} > h/2e^2$ are colored in pink and regions of $\rho_{xx} > h/e^2$ (or regions that are artificially negative owing to their extremely high resistance) are colored in purple.

The behavior of ρ_{xx} and ρ_{xy} change substantially with both n and D . There is a stripe-like region cutting diagonally across the center of the maps in Figs. 1e-f, in which one or both of ρ_{xx} and ρ_{xy} are very large.

The system is a trivial insulator for $\nu \lesssim 1/2 - 2/3$ (depending on the precise value of D), previously attributed to the formation of a Wigner crystal with period larger than the original moiré lattice [5]. There is also a pocket centered at $\nu = 2/3$ featuring large ρ_{xy} and a deep suppression of ρ_{xx} . This behavior instead indicates the formation of a topological gapped state. At $\nu = 1$, there is an extended vertical transport feature that exhibits a large anomalous Hall effect (AHE) for $0.82 \text{ V/nm} \lesssim D \lesssim 0.95 \text{ V/nm}$ but diverging ρ_{xx} with no AHE for $0.73 \text{ V/nm} \lesssim D \lesssim 0.82 \text{ V/nm}$ (see Figs. 1h-i).

To more clearly probe the nature of these states, we plot Landau fan diagrams of ρ_{xx} and ρ_{xy} for $D = 0.910 \text{ V/nm}$ and $D = 0.740 \text{ V/nm}$ (Figs. 2a and b, respectively; see Extended Data Fig. 3 for additional Landau fans from multiple voltage probes). In the former, we see a correlated Chern insulator emerging from $B = 0$ at $\nu = 1$, along with additional associated quantum Hall states emerging to its right at higher field. The line cut acquired at $B = 0.75 \text{ T}$ in Fig. 2c confirms that the correlated Chern insulator state exhibits the anticipated values of $\rho_{xx} \approx 0$ and $\rho_{xy} \approx h/e^2$, where h is Planck's constant and e is the charge of the electron. Comparison to the Streda formula [41, 42], $(\frac{\partial n}{\partial B})_\mu = C \frac{h}{e}$, further confirms that the Chern number of this state is $C = +1$, as indicated by the white dashed line shown at the top of the Landau fans. We label gapped states by their Chern number and band filling upon extrapolation to $B = 0$ following the convention ($C = a, \nu = b$) $\equiv C_b^a$, such that this state is C_1^{+1} . The insulating behavior onsets below a temperature of $T \approx 3 \text{ K}$ with a gap $\Delta_{\nu=1} = 96 \text{ } \mu\text{eV}$ ($149 \text{ } \mu\text{eV}$) at $D = 0.909 \text{ V/nm}$, determined from the temperature dependence of ρ_{xx} (ρ_{xy}) (see Extended Data Fig. 4a).

The Landau fan taken at $D = 0.740 \text{ V/nm}$ exhibits markedly different behavior. At $\nu = 1$, ρ_{xx} far exceeds h/e^2 and ρ_{xy} exhibits diverging behavior with an abrupt sign reversal across integer filling (see line cuts in Fig. 2d taken at $B = 0.20 \text{ T}$). The insulating state does not disperse with B , and associated quantum Hall states emerge roughly symmetrically to its left and right. Collectively, this behavior is consistent with a topologically trivial state, C_1^0 . The value of $D \approx 0.82 \text{ V/nm}$ where the AHE at $\nu = 1$ vanishes most likely corresponds to a phase transition between two topologically distinct states with associated Chern numbers of $C = 0$ and $+1$. Such a phase transition is typically first-order and requires a gap closure; we do not see evidence for either in our device, potentially due to disorder.

Many recent theory works [14–16, 21–29] have considered the nature of the Chern insulator previously reported at $\nu = 1$ [5]. In many other moiré systems, a correlated gap opens at $\nu = 1$ when the four-fold isospin degeneracy is lifted by interactions [33, 34]. But in RPG, the second moiré conduction band overlaps the first; as a result, this mechanism by itself would not be expected to

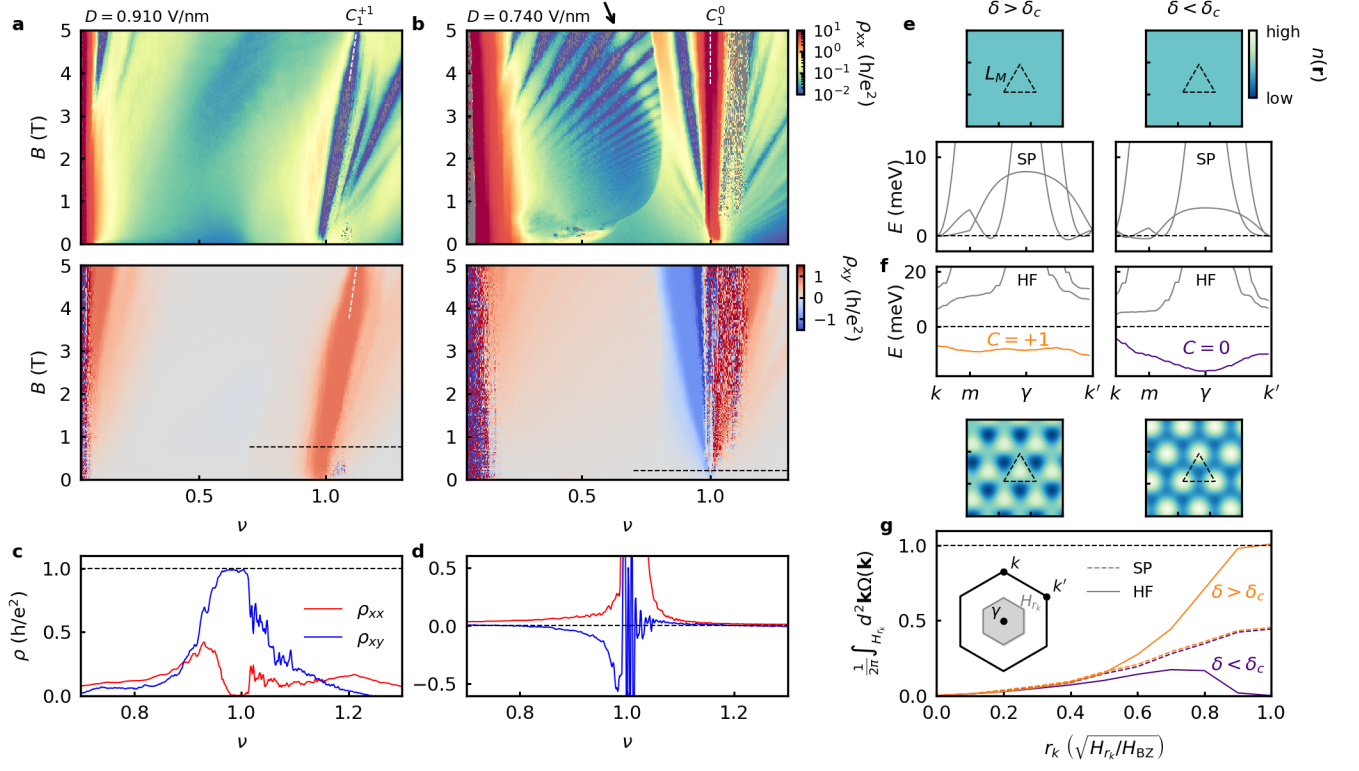


FIG. 2. **Topological and trivial electronic crystals at $\nu = 1$.** **a**, Landau fan diagram of ρ_{xx} (top) and ρ_{xy} (bottom) taken at $D = 0.910$ V/nm. The white dashed line shows the expected evolution of a $C = +1$ state originating from $\nu = 1$ based on the Streda formula. **b**, Similar Landau fan taken at $D = 0.740$ V/nm. The white dashed line shows the expected evolution of a $C = 0$ state originating from $\nu = 1$. The black arrow denotes the trajectory of a quantum Hall state with filling factor of -3 originating from $\nu = 1$. The speckled features projecting vertically near $\nu = 1$ are artifacts due to a large contact resistance. **c**, Line traces of ρ_{xx} and ρ_{xy} taken at $B = 0.75$ T from the $D = 0.910$ V/nm Landau fan, as indicated by the black dashed line in **a**. **d**, Similar line cuts taken at $B = 0.20$ T from the $D = 0.740$ V/nm Landau fan, as indicated by the black dashed line in **b**. **e**, Single-particle (SP) calculations of the spatial distribution of carrier density, $n(\mathbf{r})$, at a filling of $\nu = 1$. The left (right) panel is calculated with $\delta = 150$ meV (120 meV). Both correspond to metallic states. The associated band structure calculations are shown below each plot. The calculation is performed for a moiré period of $L_M = 11.1$ nm with the moiré potential strength artificially set to zero (see Methods). **f**, Similar calculations performed with the Hartree–Fock (HF) method. Both correspond to insulating states, with the filled band having $C = +1$ (0) for $\delta = 150$ meV (120 meV), shown in orange (purple). Dashed lines at zero energy in **e-f** denote the Fermi energy at $\nu = 1$. The real space densities in **e-f** share the same color scale. The dashed black triangles indicate the moiré unit cell. **g**, Berry curvature integrated from the center to the edge of the moiré Brillouin zone (BZ) for both values of δ considered in **e-f**. The dashed (solid) curves show the single-particle (Hartree–Fock) calculations. The inset schematic shows the moiré BZ with high symmetry points labeled. The gray area depicts the area of integration, which scales with r_k , such that $H_{r_k} = r_k^2 H_{BZ}$, where H_{BZ} is the area of the full moiré BZ.

open a gap. The AHC has thus been proposed as a new mechanism for generating a Chern insulator, in which the additional formation of an electronic crystalline order opens the topological gap [14–16, 18, 21–27]. A definitive understanding of the gap at $\nu = 1$ remains elusive, however, since the putative electronic crystal is commensurate with the moiré lattice and thus challenging to distinguish unambiguously from conventional moiré Chern insulators [43]. Nevertheless, the basic TEC framework is consistent with the $C = 1$ state we observe at $\nu = 1$. The trivial $C = 0$ insulator at smaller D can be formed by lifting the same isospin degeneracies and crystallizing

the electrons as for the AHC, but with the filled states instead having a total Chern number of zero.

To better understand the possible nature of the gapped states at $\nu = 1$, we compare our results to Hartree–Fock (HF) calculations performed with the moiré potential artificially set to zero (see Methods for details). Figures 2e–f show the calculated band structure at $\nu = 1$ both before and after HF for two different values of δ . In both cases, the state is gapless at the single-particle level but gapped as a result of interactions. The isolated band has a Chern number of $C = 0$ for δ less than a critical value of $\delta_c \approx 140$ meV, but $C = +1$ for $\delta > \delta_c$. This is consistent with our observed phase transition be-

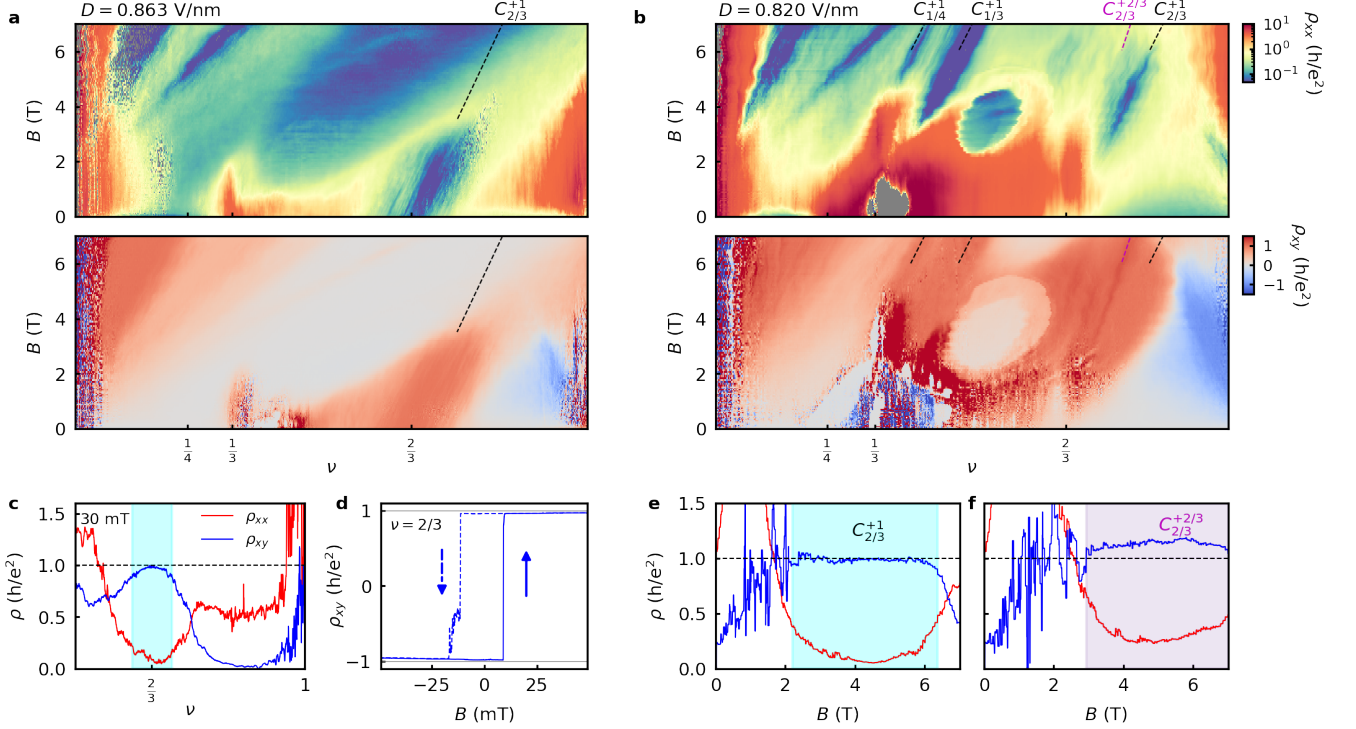


FIG. 3. **Competing TEC and FCI states at fractional ν .** **a**, Landau fan diagram of ρ_{xx} (top) and ρ_{xy} (bottom) taken at $D = 0.863$ V/nm. The black dashed line shows the expected evolution of a $C = +1$ state originating from $\nu = 2/3$ based on the Streda formula. **b**, Similar Landau fan taken at $D = 0.820$ V/nm. The black dashed lines show the expected evolution of $C = +1$ states originating from $\nu = 1/4, 1/3,$ and $2/3$. The purple dashed line shows the same for a $C = +2/3$ state originating from $\nu = 2/3$. **c**, Line traces of ρ_{xx} and ρ_{xy} taken at $B = 30$ mT from the $D = 0.863$ V/nm Landau fan in **a**. The blue shaded region corresponds to the contiguous range of ν for which $\rho_{xy} > 0.9h/e^2$. **d**, Measurement of ρ_{xy} at $\nu = 2/3$ acquired as B is swept back and forth across zero. Arrows denote the sweep direction of the magnetic field. **e**, Line traces of ρ_{xx} and ρ_{xy} taken along the trajectory indicated by the black dashed line associated with the $C_{2/3}^{+1}$ state in **b**. The blue shaded region corresponds to the contiguous region of $|\rho_{xy}| > 0.9h/e^2$ (excluding $B < 2$ T which is dominated by the trivial insulating phase). **f**, Similar line traces taken along the trajectory indicated by the purple dashed line associated with the $C_{2/3}^{+2/3}$ state in **b**. The purple shaded region corresponds to contiguous range of ν for which $\rho_{xy} > h/e^2$ (excluding $B < 3$ T).

tween a $C = 0$ and $+1$ state as D is increased. At the non-interacting level, the integrated Berry curvature up to the Fermi level at $\nu = 1$ can be any arbitrary value since the band is not isolated. Figure 2g shows that this value is $\frac{1}{2\pi} \int_{\text{BZ}} d^2\mathbf{k} \Omega(\mathbf{k}) \approx 0.5$ in the calculations for both $\delta = 120$ meV and 150 meV. When interactions open a gap, however, the filled states below the Fermi level must have Berry curvature that integrates to a quantized value, equal to C . In this context, the gap opening simultaneously necessitates an interaction-driven modification of the Berry curvature in order to satisfy the quantization condition. Small changes in the quantum geometry of the single-particle bands with δ can thus lead to an abrupt phase transition between otherwise similar states having $C = 0$ (e.g., a generalized Wigner crystal) and $C = 1$ (e.g., a generalized anomalous Hall crystal, where “generalized” indicates the role of the moiré potential in seeding the crystal formation [40, 44]). Combined with the apparent band overlap indicated by the metallic behavior

at $\nu = 4$ (Fig. 1d), this framework provides a compelling explanation for our observations at $\nu = 1$. Nevertheless, future scanning probe microscopy studies will be needed to directly confirm this interpretation.

Interplay of electronic crystals and FCI

Turning now to the correlated states at fractional band filling, we examine Landau fans acquired at intermediate values of D where noteworthy transport features are most pronounced (Figs. 3a-b for $D = 0.863$ V/nm and 0.820 V/nm, respectively). Figure 3a cuts through the largest values of R_{xy} in the $n - D$ map, and exhibits a broad region of suppressed ρ_{xx} with concomitant $\rho_{xy} \approx h/e^2$ surrounding $\nu = 2/3$ (see line cuts in Fig. 3c). At $\nu = 2/3$, ρ_{xy} switches between $\approx \pm h/e^2$ in a single hysteresis loop with a small coercive field of $B \approx 10$ mT (Fig. 3d). The slope of this state in the Landau fan is consistent with a $C = +1$ Chern insulator based on the Streda formula (i.e., $C_{2/3}^{+1}$), as indicated

by the black dashed line in Fig. 3a. These features are plainly incompatible with the $C = 2/3$ FQAH state at $\nu = 2/3$ reported previously [5], since our observed state has neither the appropriate Streda slope in the Landau fan nor the appropriate quantization of ρ_{xy} for a $C = 2/3$ state (that is, we find $\rho_{xy} = h/e^2$ rather than $3h/2e^2$). Instead, the $C_{2/3}^{+1}$ state most naturally corresponds to a TEC that spontaneously enlarges the unit cell area (see Methods for a discussion of two possible topological orders of this crystalline state). Notably, ρ_{xy} remains large over a relatively wide range of doping, potentially indicating that the crystalline order persists in some form even upon doping away from $\nu = 2/3$. The insulating behavior onsets below $T \approx 2$ K with a gap $\Delta_{\nu=2/3} = 54 \mu\text{eV}$ ($44 \mu\text{eV}$) at $D = 0.870$ V/nm, determined from the temperature dependence of ρ_{xx} (ρ_{xy}) (see Extended Data Fig. 4b).

Similar behavior is seen in the Landau fan at $D = 0.820$ V/nm, although a magnetic field is required to induce the topological phase transition from trivial to Chern insulator (see the line cut in Fig. 3e). Two additional translational symmetry-broken states with $C = +1$ emerge at even higher magnetic field, projecting to $\nu = 1/4$ and $\nu = 1/3$ at $B = 0$ (i.e., $C_{1/4}^{+1}$ and $C_{1/3}^{+1}$). There is also an oval-shaped feature near $\nu \approx 0.6$ centered at $B \approx 3.5$ T, in which both ρ_{xx} and ρ_{xy} are abruptly suppressed and there are instead quantum Hall states projecting to the CNP at $\nu = 0$. This region is separated from the surrounding area of the Landau fan by a first-order phase transition and has the same origin as the sharp curved feature in the Landau fan in Fig. 2b. This phase transition potentially reflects a collapse of the electronic crystalline order (see Methods and Extended Data Fig. 5 for additional details).

Remarkably, the Landau fan in Fig. 3b also contains an extremely narrow feature in which the antisymmetrized ρ_{xy} exceeds h/e^2 (see the line cut in Fig. 3f). The purple dashed line near the top of the Landau fan denotes the position and trajectory of this state, which projects precisely to $\nu = 2/3$ at $B = 0$ and has a Streda slope consistent with a $C = +2/3$ state (i.e., $C_{2/3}^{+2/3}$). These features are consistent with an incipient $\nu = 2/3$ FCI state emerging with B . Although the state is not fully developed, with large residual ρ_{xx} and non-quantized ρ_{xy} , the observation of $\rho_{xy} > h/e^2$ with a Streda slope implying $C = +2/3$ has no simple explanation besides a field-induced FCI state. This putative FCI appears more clearly in similar Landau fans taken at 300 mK, as well as in corresponding maps of the Hall angle, $\theta_H = \arctan(\rho_{xy}/\rho_{xx})$ (see Extended Data Figs. 6-7). The Landau fan shown in Extended Data Fig. 7 additionally carries hints of several other incipient Jain-sequence FCI states originating from $\nu = 1/3, 2/5, 3/7, 4/7,$ and $3/5$, all with $R_{xy} > h/e^2$ and a relatively large θ_H . Further hints of intermixed FCI and TEC states can be seen

in transport maps of ρ_{xx} and ρ_{xy} taken at $|B| = 2$ T (Extended Data Fig. 8), which exhibit broad regions of $\rho_{xy} > h/e^2$ with interspersed pockets of $\rho_{xy} \approx h/e^2$.

Topological states at fractional hole doping

In addition to the valley-polarized states considered so far for electron-type doping, the device exhibits a second distinct pocket of valley polarization featuring the AHE near a doping of two holes per moiré unit cell ($\nu \approx -2$). This pocket arises for $D < 0$ (gray dashed box in Fig. 1b), such that holes are pushed to the same hBN interface as for the electron-doped region considered earlier. The transport properties of this region are shown in maps taken at $B = 200$ mT (Fig. 4a). The valley-polarized pocket resides close to a trivial ($C = 0$) correlated insulator at $\nu = -2$ and slightly larger $|D|$, although the latter appears to be a completely distinct and unrelated state (see Methods). Overall, the behavior of this valley-polarized pocket is highly atypical. First, it has no particularly noteworthy features at the exact integer filling of $\nu = -2$. Instead, the predominant feature is a deep suppression of ρ_{xx} and a large enhancement of ρ_{xy} to $\approx h/4e^2$ at an incommensurate fractional filling of $\nu \approx -2.45$ (Fig. 4b). Second, a sequence of at least 10 additional oscillations in both ρ_{xx} and ρ_{xy} emerge upon reducing the hole doping. These can be seen in the maps in Fig. 4a, as well as in the line cut shown in Fig. 4b taken along the diagonal trajectory indicated by the black arrows in Fig. 4a. Third, the valley-polarized pocket appears to arise even though the highest moiré valence band is not isolated from other bands. Figure 4c shows measurements of ρ_{xx} and ρ_{xy} across a wide range of hole doping at $D = -0.096$ V/nm (see also Fig. 1b). The measurement reveals that both $\nu = 0$ and -4 remain metallic at a value of D for which the valley-polarized pocket is prominent. Combined with additional measurements revealing a complex sequence of quantum oscillations near $\nu = -2$ (Extended Data Fig. 9), we conclude that the highest moiré valence band may coexist with other moiré bands when the valley-polarized pocket is formed.

The oscillation features in the valley-polarized pocket persist to $B = 0$ (inset of Fig. 4b), although they are less clear owing to random switching of the background orbital magnetic state [45, 46]. The magnetic switching is a ubiquitous feature throughout the valley-polarized pocket, with hysteretic sign changes in ρ_{xy} driven by separately sweeping either n or D (Fig. 4d-e and Extended Data Fig. 10). Each of the oscillations corresponds to a local minimum of ρ_{xx} concomitant with a maximum of ρ_{xy} , hinting at a topological nature of these states. Landau fans reveal that these oscillatory features drift to different ν as B is raised (Figs. 4f-g), providing further evidence of their nontrivial topology. However, the properties of these states are highly unusual. The slope of each state is very large, often implying a Chern num-

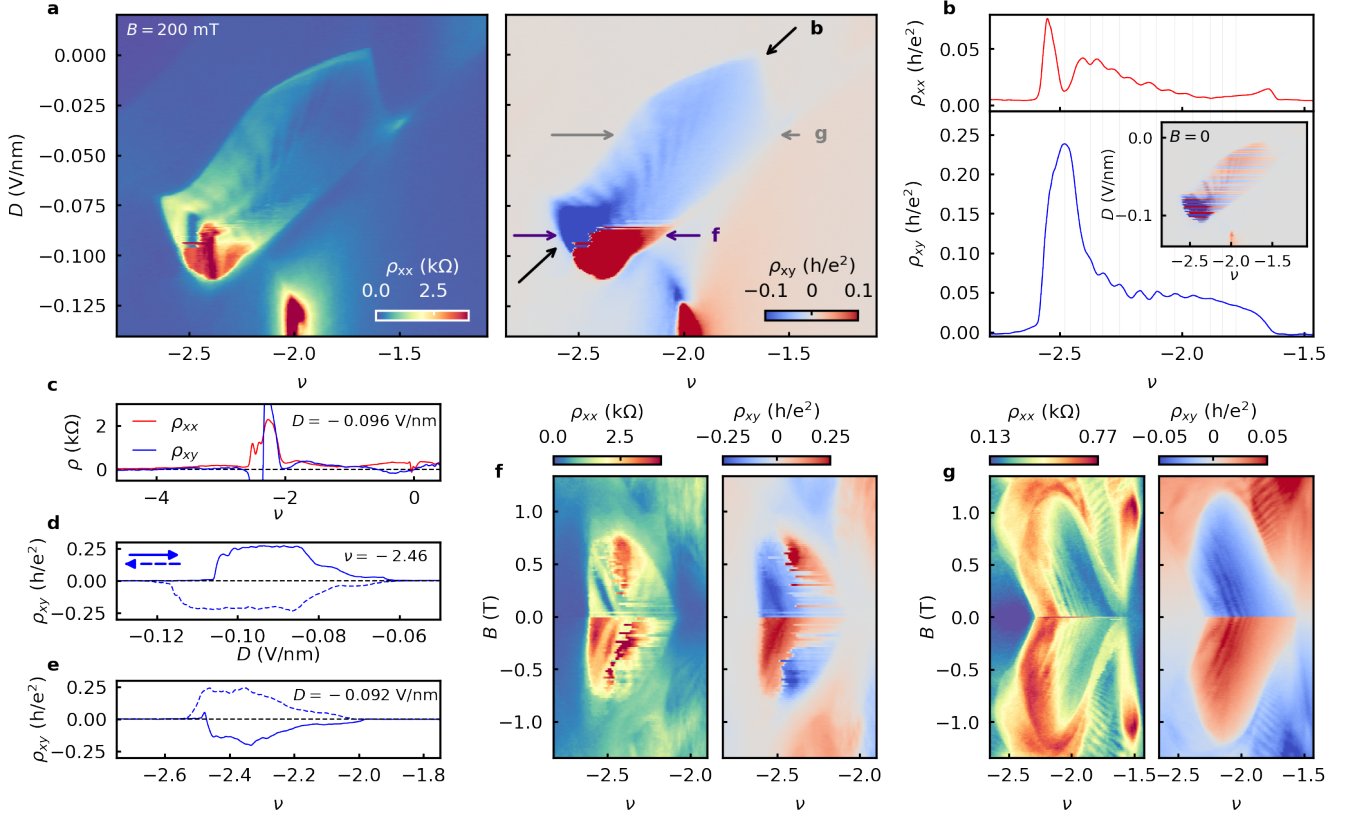


FIG. 4. **Unusual topological states in a valley-polarized pocket near $\nu = -2$.** **a**, Zoomed-in maps of ρ_{xx} (left) and ρ_{xy} (right) taken at $B = 200$ mT (not symmetrized) from the region of the gray dashed box in Fig. 1b. **b**, Line traces of ρ_{xx} and ρ_{xy} taken along a diagonal trajectory indicated by the black arrows in **a**. Vertical gray lines denote values of ν with concomitant ρ_{xx} minima and ρ_{xy} maxima. We plot the absolute value of ρ_{xy} for clarity. The inset shows the same ρ_{xy} map as in **a** but measured at $B = 0$. **c**, Line traces of ρ_{xx} and ρ_{xy} acquired at $B = 0.2$ T and $D = -0.096$ V/nm (corresponding to the position of the yellow dashed line in Fig. 1b). **d**, ρ_{xy} trace measured at fixed $\nu = -2.46$ as D is swept back and forth with $B = 0$. **e**, ρ_{xy} trace measured at fixed $D = -0.092$ V/nm as ν is swept back and forth with $B = 50$ mT. **f**, Landau fan diagram of ρ_{xx} (left) and ρ_{xy} (right) taken at $D = -0.090$ V/nm, as indicated by the purple arrows in **a**. **g**, Similar Landau fan diagram taken at $D = -0.040$ V/nm, as indicated by the gray arrows in **a**.

ber as large as 13 based on a naive application of the Streda formula. These trajectories are also not perfectly linear, indicating a breakdown of the applicability of the Streda formula. Additionally, whereas the primary state remains pinned to $\nu \approx -2.45$ upon varying D , all of the other states bear no fixed relationship between ν and D . Instead, they exhibit non-uniform spacing and drift as a function of D with no easily quantifiable pattern.

Although the nature of these states remains both mysterious and unprecedented in comparison to all previously known Chern insulators, we speculate on a possible explanation of their origin. In a simple model with band overlap, itinerant carriers from other bands can remain at the Fermi surface even when a valley-polarization gap opens in the highest moiré valence band. This multi-band behavior could explain the non-quantized ρ_{xy} and large residual ρ_{xx} , since the topological protection of the gapped states is spoiled by itinerant carriers in other

bands. Such a scenario also necessitates modifying the Streda formula, as described in the Methods, which could explain the nonlinear trajectories of some of these states in the Landau fans. Finally, it implies that the nominal value of ν in fact reflects the total filling of all the relevant subbands, rather than the highest moiré valence band alone. In such a picture, the primary state seen at $\nu \approx -2.45$ may actually correspond to a filling of precisely two holes per moiré unit cell in the highest moiré valence band, with the remaining holes residing in the overlapping bands. The sequence of additional states arising at reduced hole doping may be a periodic recurrence of the primary Chern state, arising as interactions induce non-uniform charge transfer between the bands [47].

Discussion and outlook

Overall, our results establish moiré RPG as a promising platform for investigating the interplay between TEC

and FCI states. Understanding their relationship stands as a critical open challenge for the field, especially as it relates to determining the ultimate ground state ordering of the system. Our observations further motivate the tantalizing possibility of finding topological states with coexisting charge fractionalization and electronic crystallization. Understanding the dependence of the TEC and FCI states on the moiré period, as well as studying the impact of Coulomb screening [48], may help to further elucidate their relationship.

In our measurements, we find likely TEC states at both fractional and integer fillings forming above $D \approx 0.82 - 0.87$ V/nm (depending on ν). The most likely ground state for smaller D is a generalized Wigner crystal with $C = 0$, but this undergoes a phase transition to various topological phases above $B \approx 1 - 3$ T (depending on D , see Figs. 1e-g, Figs. 3a-b, and Extended Data Figs. 6-8). These topological phases arise as intermixed integer and incipient fractional Chern insulators, pointing to a close and possibly intertwined relationship between the two. Notably, the putative generalized Wigner crystal extends over the largest range of D very near $\nu = 1/3$ (Fig. 1e). Similarly, both $C = 0$ and $C = +1$ insulators appear most robustly very near $\nu = 2/3$ and $\nu = 1$ (Figs. 2a-b and Fig. 3a), collectively indicating that the electronic crystals are most stable at commensurate fillings of the moiré lattice.

Looking forward, we note that the competing trivial and topological electronic crystals at a given ν are likely to feature different spatial structures owing to the delocalized nature of the topological states in real space (see Fig. 3f). Scanning probe studies will be crucial for directly imaging the electronic crystals and better understanding the nature of their doping-dependent translational symmetry breaking. The other pocket of valley-polarization near two holes per moiré unit cell also holds many intriguing mysteries, featuring signatures of unusual topological behaviors not previously seen in other systems. Twist-angle-dependent studies will be valuable, as this pocket may share the same origin as the multiferoic ‘bubble’ region previously studied in RPG without a moiré [49]. From this perspective, the addition of the moiré potential may primarily serve to trigger the formation of a peculiar sequence of topological states within the valley-polarized pocket. Whether electronic crystallization is also needed to form these states stands as an open question for future study.

METHODS

Identification of rhombohedral domains. We identified five-layer thick flakes of exfoliated graphene using an optical microscope. We then mapped the stacking domains (e.g., Bernal and rhombohedral, along with other less energetically favorable configurations) with

amplitude-modulated Kelvin probe force microscopy (AM-KPFM) using a Bruker Icon atomic force microscope (AFM) with an SCM-PIT-V2 tip (see Extended Data Fig. 1). We applied an ac voltage bias to the tip between 500 – 1500 mV and reduced the tip-sample separation by 5 – 10 nm compared to the average height of the tapping mode. These parameters were adjusted during measurement in order to optimize the signal contrast. The tapping mode topography and AM-KPFM measurements were interleaved, such that the topography was collected during one raster direction of the tip and the AM-KPFM potentiometry was performed during the reverse raster scan (with the tip held at a constant tip-sample separation based on the measured topography). Although the graphene flake was not electrically grounded, which should preclude the applicability of AM-KPFM, we were nevertheless able to distinguish very clear contrast in the measured signal for different stacking domains. We could further confirm that a given domain of interest was indeed rhombohedral by comparing a Raman spectrum taken with a 514 nm laser to the Bernal region along with other published curves [50]. The process is shown in more detail in Supplementary Information Fig. S1. The $C = -5$ Chern insulator seen in the Landau fan in Extended Data Fig. 2 provides additional confirmation of both the layer number and rhombohedral stacking configuration of the graphene flake [50].

Device fabrication. The RPG region of interest was first isolated using a resist-free local anodic oxidation nanolithography process [51], substantially reducing the chance that it relaxed into the energetically-favored Bernal stacking configuration as it was picked up into the vdW stack. In order to further reduce the risk of relaxation, we separately prepared the bottom portion of the stack by picking up an hBN and graphite dielectric/back-gate and placing them onto an SiO₂ substrate. We then cleaned the surface of the hBN using contact-mode AFM (using a OTESPA-R3 AFM tip and a line spacing of ≈ 100 nm). This pre-assembly procedure allowed us to deposit the top half of the stack — graphite/hBN/RPG — as the last step of the vdW heterostructure assembly process, mitigating the risk of relaxing the rhombohedral flake upon further straining the crystal while picking up additional vdW flakes [52]. For all steps of stacking, we used standard dry transfer techniques with a polycarbonate (PC) film on a polydimethyl siloxane (PDMS) stamp.

Straight edges of the RPG were aligned to the top and bottom hBN, such that there was a 50% chance of either hBN creating a long-wavelength moiré potential. We note that this technique led to an unintentional ambiguity in determining which hBN interface is aligned, as both in principle could be. Since the transport features of our device closely resemble many of those seen in Ref. [5], we assume that we most likely have the same polarization scheme (i.e., both electrons and holes biased to the

RPG surface away from the aligned hBN moiré interface in their respective valley-polarized pockets) and infer that the top hBN creates the long-wavelength moiré pattern. We only observe signatures of a single long-wavelength moiré pattern in the transport data up to a doping of $n = 11.59 \times 10^{12} \text{ cm}^{-2}$ (Supplementary Information Fig. S2), setting a lower bound on the twist angle of the misaligned hBN of 2.03° and an upper bound on the shorter moiré period of 6.31 nm.

After stacking, standard device fabrication procedures were employed to create the dual-gated Hall bar device (i.e., reactive ion etching and evaporation of 7/70 nm of Cr/Au, all using poly(meth)acrylate (PMMA) masks patterned by e-beam lithography). Extended Data Fig. 1a shows an optical micrograph of the completed device. Contacts are labeled in the image to indicate the specific electrodes used to perform the transport measurements.

Transport measurements. Transport measurements were carried out across two thermal cycles, first in a Bluefors LD dilution refrigerator equipped with a 3-axis superconducting vector magnet and then in a Bluefors XLD dilution refrigerator with a one-axis superconducting magnet. In both systems, the nominal base mixing chamber temperature was $T = 10 - 20 \text{ mK}$, as measured by a factory-supplied RuO_x sensor. Unless otherwise specified, measurements were carried out at the nominal base temperature of the fridge. Four-terminal lock-in measurements were performed by sourcing a small alternating current of either $I_{ac} = 120 \text{ pA}$ or 1.0 nA at a frequency $< 20 \text{ Hz}$, chosen to accurately capture sensitive transport features while minimizing electronic noise. In addition, a global bottom gate voltage between -120 V and $+60 \text{ V}$ was applied to the Si substrate to improve the contact resistance. Data in Figure 4 was acquired with $I_{ac} = 1.0 \text{ nA}$. Unless otherwise specified, all others were taken with $I_{ac} = 120 \text{ pA}$.

The charge carrier density, n , and the out-of-plane electric displacement field, D , were defined according to $n = (C_{bg}V_{bg} + C_{tg}V_{tg})/e$ and $D = (C_{tg}V_{tg} - C_{bg}V_{bg})/2\epsilon_0$, where C_{tg} and C_{bg} are the top and bottom gate capacitance per unit area and ϵ_0 is the vacuum permittivity. C_{tg} and C_{bg} were estimated by fitting the slopes of the quantum Hall states in the Landau fan shown in Extended Data Fig. 2b.

To reduce geometric mixing between measured longitudinal and transverse voltage when $|B| > 0$, we often plot the field-symmetrized values of resistance. ρ_{xx} was symmetrized according to $(\rho_{xx}(B > 0) + \rho_{xx}(B < 0))/2$, and ρ_{xy} was antisymmetrized according to $(\rho_{xy}(B > 0) - \rho_{xy}(B < 0))/2$. All of the measurements are (anti-)symmetrized, unless otherwise specified.

The contacts are labeled in the schematic in Extended Data Fig. 1a. Contacts A and B were used as the source and drain electrodes. All measurements of ρ_{xy} were made

using contacts 2 and 4. Measurements of ρ_{xx} were made using contacts 1 and 2 (Figs. 1e-i, 2a-d, 3b, and 3e-f), or 2 and 3 (Fig. 1d, 3a, 3c-d, and 4). The RPG/hBN twist angle extracted from the two pairs of voltage probes is identical within experimental resolution, although contact-specific artifacts differ between the pairs (e.g., see Extended Data Fig. 3). In all Extended Data and Supplementary Information Figures, we denote which contact pair is being shown. The map in Fig. 1b was constructed by summing the signal between contacts 1-2 and 2-3 and dividing by 2 in order to mitigate contact-specific artifacts. The map was taken piece-wise and stitched together post-measurement, with the voltage on the silicon gate adjusted appropriately for each segment of the map in order to best eliminate contact resistance artifacts.

Determination of moiré period and twist angle. The carrier density, n_s , required to fully fill a four-fold degenerate moiré band was estimated by fitting the sequence of Brown-Zak oscillations from a Landau fan taken at $D = 0$, as shown in Extended Data Fig. 2. The oscillations occur when $\phi/\phi_0 = 4B/n_s\phi_0 = p/q$, where $\phi_0 = h/e$ is the magnetic flux quantum and p and q are integers. The value of n_s is confirmed by fitting the sequences of quantum Hall states arising from the fully-filled moiré bands (i.e., four electrons or holes per moiré unit cell). Using n_s , the filling factor ν was defined according to $\nu = n/(n_s/4)$. The superlattice density is related to the moiré wavelength by $L_M = \sqrt{8/\sqrt{3}n_s}$, from which we find the twist angle according to the equation

$$L_M(\theta, a_G, \delta_a) = \frac{(1 + \delta_{a_G}) \cdot a}{\sqrt{2} \cdot (1 + \delta_a) \cdot (1 - \cos \theta) + \delta^2}$$

where $a_G = 0.246 \text{ nm}$ is the lattice constant of graphene, θ is the twist angle between the hBN and the RPG, and $\delta_a = \frac{a_{\text{hBN}} - a_G}{a_{\text{hBN}}} \approx 0.017$ is the lattice mismatch between the lattice constants of the hBN (a_{hBN}) and graphene. We note that the conversion to twist angle depends on the choice of the lattice mismatch between graphene and hBN, which is not precisely known. For consistency with prior work [5], we chose a value of 1.7%. There are also two distinct stacking configurations of RPG and hBN resulting in a long-wavelength moiré potential, in which the RPG is aligned with hBN close to either 0° or 60° [18]. We are unable to distinguish between these possibilities experimentally, or know whether our sample has the same or opposite sense of the alignment compared with that in Ref. 5. All of the calculations are performed assuming a configuration in which the A and B sublattices of the aligned graphene layer reside close to the nitrogen and boron atoms of the hBN, respectively. Despite the inherent ambiguities in extracting the twist angle, we emphasize that there is no ambiguity in extracting the moiré period as it can be converted directly from the value of n_s with no free parameters.

Analysis of the full transport map. Here, we de-

tail the salient features in the transport map shown in Fig. 1b. At the charge neutrality point (CNP, $\nu = 0$), there is an insulating state surrounding $D = 0$ marked by diverging ρ_{xx} . This insulator has previously been understood to arise as a consequence of a correlation-driven layer-antiferromagnetic state [50, 53–57]. As $|D|$ is raised, the insulator collapses to a semimetallic state and then reemerges as a band insulator due to a single-particle band gap formed at the CNP. At $\nu = \pm 4$, there are features with higher resistance than at nearby doping, suggestive of a strongly suppressed density of states or small gaps opening upon fully filling the four-fold (spin and valley) degenerate moiré valence and conduction bands. This behavior arises over a small range of $D > 0$ for $\nu = -4$, and over a larger range of D for $\nu = +4$.

Highly resistive states also appear at integer filling factors $\nu = 1, 2$, and 3 for electron-type doping, as well as at $\nu = -2$ for hole-type doping. These are correlated insulating states, formed as a consequence of strong interactions within the moiré flat bands that lift the spin and valley degeneracies. For electron-type doping, these states are more prominent for $D < 0$, corresponding to electrons biased towards the moiré interface. The corresponding states at $D > 0$ are insulating over smaller ranges of D , perhaps reflecting the weaker moiré potential experienced by electrons biased away from the moiré interface.

There are many other resistive features in the map that drift through the $n - D$ parameter space, with no apparent tie to precise integer ν . These features most likely reflect metallic van Hove singularities (vHs) formed within the moiré minibands. These could correspond either to vHs within the non-interacting bands, or to interaction-driven vHs arising when isospin degeneracies are spontaneously broken through a generalized Stoner instability. Many of these features are prevalent in RPG without an hBN moiré [49]. In this sense, the moiré potential can be viewed as acting to trigger the formation of insulating states when such vHs features drift close to integer values of ν . Such behavior has been seen previously for aligned vs. misaligned rhombohedral trilayer graphene [52].

For $\nu > 0$ and large $D < 0$, and also for $\nu < 0$ and large $D > 0$, there are expansive regions of immeasurably large resistance. These regions can sometimes correspond to negative resistance in our four-terminal transport measurements. Such behavior is often seen adjacent to very insulating states in vdW devices, generally corresponding to regimes of percolative transport where the electrical potential between voltage probes is not well defined. There is also an artifact that cuts diagonally through the map, crossing through the insulator at $\nu = -2$ and $D > 0$ and intersecting $\nu = D = 0$. Unlike other artifacts driven by poor equilibration with the contacts, changing the silicon gate modifies its location in $n - D$ space but does not suppress it completely (see Fig. 1b vs. Fig. S2). We

currently do not know the origin of this artifact, but note that it is nearly parallel to the V_{tg} axis and that similar features are routinely seen in 4–6 layer rhombohedral graphene devices, e.g. Refs. 5, 50, and 58.

First-order phase transition at fractional electron-doped band filling. An intriguing feature of the Landau fan shown in Fig. 2b is the first-order phase transition that curves from $\nu \approx 0.2$ near $B = 0$ to $\nu \approx 0.75$ at $B = 5$ T (see Extended Data Fig. 5). This phase transition separates very different quantum Hall states in the ρ_{xx} Landau fan, and at large B corresponds to an abrupt sign reversal in ρ_{xy} . There are quantum oscillations on either side of the phase transition with an apparent degeneracy of 1, indicating that spin and valley are likely polarized in both cases. It is possible that the overdoped side of the phase transition corresponds to the electronic crystal state responsible for the insulator at $\nu = 1$, whereas the underdoped side corresponds to a situation in which the crystalline order has collapsed and there is overlap between the lowest and next higher moiré conduction band. In this scenario, only a single spin–valley branch of the lowest moiré conduction band is filled, whereas the next dispersive band may remain unpolarized. The quantum Hall state arising from $\nu = 1$ with Landau level filling factor $\nu_{LL} = -3$ (indicated by the black arrow in Fig. 2b) provides evidence for this interpretation, as the state appears to be gapped on the overdoped side of the phase transition but gapless on the underdoped side. In the latter case, it is responsible for only weakly modulating the resistance of the partially filled Landau levels emerging from $\nu = 0$. More work is needed to better understand the nature of this first-order phase transition and the evolution of the fermiology of surrounding states as a function of doping. However, it is interesting to note that a remarkably similar feature is seen in twisted bilayer-trilayer graphene [40], which also hosts TEC states that spontaneously break the discrete translational symmetry of the moiré lattice.

Correlated insulators at $\nu = -2$. In addition to the pocket of valley-polarization near $\nu = -2$ shown in Fig. 4, there are also incipient correlated insulating states precisely at $\nu = -2$ over a narrow range of both signs of D . These states appear to arise independently from the valley-polarized pocket, despite their close proximity in the $n - D$ map. The nature of these incipient insulators is not entirely clear. The states appear to be trivial insulators, with $C = 0$, based on analysis of Landau fan diagrams taken at fixed D (Extended Data Fig. 9). The resistance of the states grows rapidly with increasing B , but becomes only slightly larger with magnetic field oriented in the 2D plane up to 1 T. The absence of Chern insulator behavior and associated AHE upon doping appears to be inconsistent with valley polarization. The weakly growing resistance with in-plane field is consistent with spin-polarized insulators, although it appears that the accessible 1 T range of in-plane field is not sufficient

to unambiguously determine the ground state ordering. Curiously, these states arise only over values of D for which the CNP is in a semimetallic state, although it is not clear whether this is meaningful or purely a coincidence. Future work will be needed to better understand the nature of these incipient correlated insulating states, and whether they have any meaningful interplay with the nearby pocket of valley polarization.

Modification of Streda formula for gapless states. As discussed in the main text, the trajectories of the incipient Chern insulator states in the Landau fans in Figs. 4f-g are atypical in that they are: (i) occasionally curved, (ii) imply Chern numbers that are larger than the apparent value extracted from the maximum value of ρ_{xy} , and (iii) can have anomalously large values as big as 13. All of these features call into question the applicability of the Streda formula in assigning a Chern number to these states. In particular, there is no simple explanation for the observation of a Streda slope that is larger than the Chern number implied by ρ_{xy} , as this behavior cannot easily be ascribed to effects of disorder (which can artificially reduce, but never enhance, the value of the antisymmetrized ρ_{xy} in an incipient Chern insulator). The most notable disagreement lies in the “primary” state at $\nu \approx -2.45$, which has an apparent Streda slope of 7 but $\rho_{xy} \approx h/4e^2$ implying a Chern number of 4 (see Figs. 4b and f).

However, if there are coexisting itinerant charges residing in additional bands, the system is not in a fully gapped state and the Streda formula is not applicable. In this situation, an additional contribution related to Hall diffusion must be taken into account [59]. In the most general scenario, tracking the evolution of a given topological state necessitates considering how the state evolves with both B and μ , where μ is the chemical potential: $dn = \left(\frac{\partial n}{\partial B}\right)_\mu dB + \left(\frac{\partial n}{\partial \mu}\right)_B d\mu$. The first term here describes the usual Streda formula, whereas the second arises due to the coexisting itinerant charges. We do not attempt to understand the precise trajectories of the incipient Chern insulators, but speculate that the anomalous slopes of the states we observe may originate from the additional contribution of coexisting itinerant charges in overlapping bands. Such a scenario likely requires that the itinerant charges have low mobility, such that they do not completely suppress the characteristic deep minima in ρ_{xx} and large enhancements of ρ_{xy} arising from the chiral edge modes and incompressible bulk of the Chern insulator formed in the highest moiré valence band.

Quantum oscillations induced by graphite gates. Some of the Landau fan diagrams exhibit periodic oscillations as a function of B that do not depend on ν (e.g., Fig. 3b). These are not consistent with Brown-Zak oscillations given the known moiré period of the sample. Instead, they appear to arise as a consequence of cyclotron gaps formed on the surface of

the graphite gates. Supplementary Information Fig. S3 shows a Fourier transform analysis of these oscillations for various different Landau fan diagrams. Oscillations are seen across a wide range of ν and D , but all have similar frequencies of $f_B \approx 33$ T. This behavior is most prominent in regions of the Landau fans where the resistance changes rapidly with gate voltage (i.e., large dR/dn). Collectively, this behavior is consistent with that seen in a previous study of graphite-gated vdW heterostructures, pointing to their origin as oscillations in the graphite density of states [60]. Therefore, all such oscillations appearing at fixed B over a wide range of ν most likely originate from the graphite gates, and do not reflect the intrinsic physics of moiré RPG.

Dependence of the transport properties of TEC states on bias current. The transport properties of the Chern insulators in the electron-doped valley-polarized pocket are extremely sensitive to the bias current. Supplementary Information Fig. S6 shows measurements of ρ_{xx} and ρ_{xy} taken as a function of dc current bias, I_{dc} . To perform these measurements, the dc current is applied in addition to a small ac bias of 14 pA while measuring the differential resistance, dV/dI , with a lock-in amplifier. Supplementary Information Fig. S6b shows representative line traces taken for the Chern insulators at $\nu = 2/3$ and 1. Both show that ρ_{xy} deviates from its (nearly) quantized value as I_{dc} is raised. Similarly, ρ_{xx} quickly transitions from a deep minimum to a large value close to h/e^2 . Supplementary Information Fig. S6c show maps of ρ_{xx} and ρ_{xy} vs. I_{dc} measured across a range of ν . The maps show that both quantities are especially sensitive to even small increases in I_{dc} within the Chern insulator states, but less sensitive in metallic states.

Band structure calculation. We use the continuum model to calculate the band structure. The Hamiltonian for each valley and spin is:

$$H_K = H_0 + H_M, \quad (1)$$

where H_0 is the Hamiltonian of rhombohedral pentalayer graphene:

$$H_0 = \begin{pmatrix} H_1 & \Gamma & \tilde{\Gamma} & \mathbf{0}_{2 \times 2} & \mathbf{0}_{2 \times 2} \\ \Gamma^\dagger & H_2 & \Gamma & \tilde{\Gamma} & \mathbf{0}_{2 \times 2} \\ \tilde{\Gamma}^\dagger & \Gamma^\dagger & H_3 & \Gamma & \tilde{\Gamma} \\ \mathbf{0}_{2 \times 2} & \tilde{\Gamma}^\dagger & \Gamma^\dagger & H_4 & \Gamma \\ \mathbf{0}_{2 \times 2} & \mathbf{0}_{2 \times 2} & \tilde{\Gamma}^\dagger & \Gamma^\dagger & H_5 \end{pmatrix}, \quad (2)$$

with

$$H_i = \begin{pmatrix} \left(\frac{i}{4} - \frac{1}{2}\right)\delta & -\frac{\sqrt{3}}{2}\gamma_0(\tilde{k}_x - i\tilde{k}_y) \\ -\frac{\sqrt{3}}{2}\gamma_0(\tilde{k}_x + i\tilde{k}_y) & \left(\frac{i}{4} - \frac{1}{2}\right)\delta \end{pmatrix}, \quad (3)$$

$$\Gamma = \begin{pmatrix} -\frac{\sqrt{3}}{2}\gamma_4(\tilde{k}_x - i\tilde{k}_y) & -\frac{\sqrt{3}}{2}\gamma_3(\tilde{k}_x + i\tilde{k}_y) \\ \gamma_1 & -\frac{\sqrt{3}}{2}\gamma_4(\tilde{k}_x - i\tilde{k}_y) \end{pmatrix}, \quad (4)$$

$$\tilde{\Gamma} = \begin{pmatrix} 0 & \frac{1}{2}\gamma_2 \\ 0 & 0 \end{pmatrix}, \quad (5)$$

where the parameters are $(\gamma_0, \gamma_1, \gamma_2, \gamma_3, \gamma_4) = (-2600, 358, -8.3, 293, 144)$ meV. δ is the potential difference between the top and the bottom graphene layers. $\tilde{k}_x + i\tilde{k}_y = e^{i\theta_3}(k_x + ik_y)$, where $\theta_3 = \arctan \frac{\theta}{\delta_\alpha}$. The moiré potential is:

$$H_M(\mathbf{G}_j) = \begin{pmatrix} C_0 e^{i\phi_0} + C_z e^{i\phi_z} & C_{AB} e^{i(\frac{5-j}{3}\pi - \phi_{AB})} \\ C_{AB} e^{i(\frac{3+j}{3}\pi - \phi_{AB})} & C_0 e^{i\phi_0} - C_z e^{i\phi_z} \end{pmatrix}, \quad (6)$$

which represents the tunneling in the first graphene layer aligned with the hBN, with momentum difference given by $\mathbf{G}_j = \frac{4\pi}{\sqrt{3}L_M}(\cos(\frac{j\pi}{3} - \frac{5\pi}{6}), \sin(\frac{j\pi}{3} - \frac{5\pi}{6}))^T$, $j = 1, 3, 5$. For $j = 2, 4, 6$, the tunneling can be determined by taking the Hermitian conjugate. The parameters are determined from DFT calculations [61] as $C_0 = -10.13$ meV, $\phi_0 = -86.53^\circ$, $C_z = 9.01$ meV, $\phi_z = -8.43^\circ$, $C_{AB} = 11.34$ meV, $\phi_{AB} = -19.60^\circ$.

Hartree–Fock calculations. We perform Hartree–Fock calculations for $\nu = 1$ with a moiré period of 11.1 nm. The BZ used is the moiré BZ. The Coulomb interaction term is expressed as:

$$H_{\text{int}} = \frac{1}{2A} \sum_{\mathbf{q}} \sum_{l, l'} V_{l, l'}(\mathbf{q}) : \rho_l(\mathbf{q}) \rho_{l'}(-\mathbf{q}) :, \quad (7)$$

where $\rho_l(\mathbf{q})$ represents the electron density at layer l , and A denotes the system area. The interaction potential is written as:

$$V_{l, l'}(\mathbf{q}) = \frac{e^2 e^{-q|l-l'|d_{\text{layer}}} \tanh(q\lambda)}{2\epsilon\epsilon_0 q}, \quad (8)$$

with $d_{\text{layer}} = 0.34$ nm being the distance between adjacent layers, $\lambda = 30$ nm the screening length and $\epsilon = 10$ the dielectric constant. We consider four conduction bands in the BZ at the single-particle level and carry out self-consistent calculations. We evaluate 100 random initial ansatzes and choose the one with the lowest energy.

We note that our HF calculations are unable to reproduce the transition between $C = 0$ and $C = 1$ gapped states at $\nu = 1$ for a moiré period of 10.8 nm. Such a transition can be captured either by slightly increasing the moiré period to at least 11.3 nm, or by increasing it to 11.1 nm and artificially setting the moiré potential strength to zero. The origin of this disagreement is currently not clear, and will require further investigation to understand. In order to illustrate a possible physical origin of this topological phase transition, we show calculations in Fig. 2e-g in the limit of a vanishing moiré potential for a moiré period of 11.1 nm. These calculations are meant to motivate a possible mechanism for generating the transition between $C = 0$ and $C = +1$ states at $\nu = 1$, rather than perfectly capture the physics of the system. The calculations for the case of the 11.3 nm moiré period and non-zero moiré potential are qualitatively consistent with the results shown in Figs. 2e-g;

thus, the inclusion or exclusion of the weak moiré potential does not meaningfully impact the conclusions of this analysis.

Spatial charge distribution calculation. The spatial distribution $n(\mathbf{r})$ is defined as $\langle c^\dagger(\mathbf{r})c(\mathbf{r}) \rangle$, where $c(\mathbf{r})$ is the electron operator in real space. $n(\mathbf{r})$ is calculated by:

$$\begin{aligned} n(\mathbf{r}) &= \sum_{\mathbf{q}} n(\mathbf{q}) e^{-i\mathbf{q}\cdot\mathbf{r}} \\ &= \frac{1}{N_1 N_2} \sum_{\mathbf{k}} \sum_{\mathbf{q}} \langle u(\mathbf{k} + \mathbf{q}) | u(\mathbf{k}) \rangle e^{-i\mathbf{q}\cdot\mathbf{r}}, \end{aligned} \quad (9)$$

where k is defined in the BZ, which is discretized into $N_1 \times N_2$ points. $|u(\mathbf{k} + \mathbf{q})\rangle$ is the periodic part of the Bloch wavefunction. Here, $\mathbf{q} = n_1 \mathbf{G}_1 + n_2 \mathbf{G}_2$ represents any integer linear combination of the crystal reciprocal lattice vectors. The unit of $n(\mathbf{r})$ is the area of the BZ divided by $4\pi^2$.

Berry curvature and Chern number calculation. We calculate the Berry curvature using the method from Ref. 62. The BZ is discretized into an $N_1 \times N_2$ grid. For each \mathbf{k} in the BZ, we calculate the $U(1)$ link:

$$U_\mu(\mathbf{k}) = \langle u(\mathbf{k} + \delta k_\mu \hat{\mathbf{k}}_\mu) | u(\mathbf{k}) \rangle, \quad (10)$$

where $\mu = 1, 2$. The Berry curvature is then given by:

$$\Omega(\mathbf{k}) = \frac{\arg W(\mathbf{k})}{\delta k_1 \delta k_2}, \quad (11)$$

where $W(\mathbf{k})$ is $U_1(\mathbf{k})U_2(\mathbf{k} + \delta k_1 \hat{\mathbf{k}}_1)U_1^{-1}(\mathbf{k} + \delta k_2 \hat{\mathbf{k}}_2)U_2^{-1}(\mathbf{k})$. We ensure that $-\pi < \arg W(\mathbf{k}) \leq \pi$. The Chern number is calculated as:

$$C = \frac{1}{2\pi} \int_{\text{BZ}} d^2\mathbf{k} \Omega(\mathbf{k}). \quad (12)$$

In Fig. 2g, the flux is calculated as:

$$\frac{1}{2\pi} \int_{H_{r_k}} d^2\mathbf{k} \Omega(\mathbf{k}), \quad (13)$$

where H_{r_k} corresponds to the moiré BZ scaled by r_k , with $r_k = 1$ recovering the original moiré BZ.

Possible ground state orderings at $\nu = 2/3$. We consider three possible states at $\nu = 3$: (I) A FQAH state with the crystal lattice matching the moiré wavelength L_M ; (II) A crystal state with a period $L_{\text{crystal}} = L_M/\sqrt{2/3}$ in which one folded band is fully filled; (III) A different crystal state with a period $L_{\text{crystal}} = L_M/\sqrt{1/3}$ in which two folded bands are fully filled. Both (II) and (III) describe states that can be thought of as (generalized) anomalous Hall crystals, differing primarily by the sizes of their unit cells.

For (I), we first perform a Hartree–Fock calculation at $\nu = 1$, followed by an exact diagonalization study by projecting the Coulomb interaction into the lowest HF

band [15]. For (II), we perform a Hartree–Fock calculation in a BZ scaled by $\sqrt{2/3}$ compared to the moiré BZ, with one electron per unit cell. We manually switch off the moiré potential due to its incommensurability with the crystal period. For (III), we perform a Hartree–Fock calculation in a BZ scaled by $1/\sqrt{3}$ compared to the moiré BZ, with two electrons per unit cell. Supplementary Information Fig. S13 shows HF band structure calculations illustrating the difference between the TEC states (II) and (III). To the best of our knowledge, these two forms of TEC are indistinguishable in our transport measurements, since both manifest as identical $C = 1$ Chern insulators on the device scale. These states could potentially be distinguished by microscopically imaging the electronic crystal owing to their different unit cell sizes. Our HF modeling predicts that states (I), (II), and (III) differ in energy by less than 0.65 meV per moiré unit cell. Therefore, at this point it is not possible to determine the ground state with any realistic degree of confidence. We thus caution that more experimental and theoretical work is needed to fully capture the physics of the phase at $\nu = 2/3$.

ACKNOWLEDGEMENTS

The authors thank Long Ju for sharing preliminary data; Hart Goldman, Trithep Devakul, Justin Song, and David Cobden for helpful discussions; Yinong Zhang, Jordan Fonseca, and Jiaqi Cai for technical assistance with the AM-KPFM imaging of graphene stacking domains. Research at the University of Washington on correlation-driven topology in pentalayer graphene was solely supported as part of Programmable Quantum Materials, an Energy Frontier Research Center funded by the U.S. Department of Energy (DOE), Office of Science, Basic Energy Sciences (BES), under award DE-SC0019443. Experiments at the University of British Columbia were undertaken with support from the Natural Sciences and Engineering Research Council of Canada; the Canada Foundation for Innovation; the Canadian Institute for Advanced Research; the Max Planck-UBC-UTokyo Centre for Quantum Materials and the Canada First Research Excellence Fund, Quantum Materials and Future Technologies Program; and the European Research Council (ERC) under the European Union’s Horizon 2020 research and innovation program, Grant Agreement No. 951541. D.W. was supported by an appointment to the Intelligence Community Postdoctoral Research Fellowship Program at University of Washington administered by Oak Ridge Institute for Science and Education through an interagency agreement between the US Department of Energy and the Office of the Director of National Intelligence. M.Y., X.X., and A.O. acknowledge support from the State of Washington-funded Clean Energy Institute. K.W. and T.T. acknowl-

edge support from the JSPS KAKENHI (Grant Numbers 21H05233 and 23H02052) and World Premier International Research Center Initiative (WPI), MEXT, Japan. This work made use of shared fabrication facilities at UW provided by NSF MRSEC 2308979 with graphene device development supported by National Science Foundation (NSF) CAREER award no. DMR-2041972. Theoretical calculations were supported by the National Science Foundation under Grant No. DMR-2237031. This work acknowledges usage of the millikelvin optoelectronic quantum material laboratory supported by the M. J. Murdock Charitable Trust.

AUTHOR CONTRIBUTIONS

A.O. and D.W. developed the sample fabrication capabilities; A.O. fabricated the sample; D.W. and A.O. measured the sample in the Yankowitz lab at UW; R.S. performed follow-up measurements in the Folk lab at UBC, which appear in many of the main text figures, under the supervision of J.F. and in discussion with D.W., A.O., and M.Y.; D.W. and A.O. analyzed the data with the assistance of R.S.; J.Y. developed the AFM-based imaging technique to detect rhombohedral graphene under the supervision of X.X.; M.Y. supervised the project; D.W., A.O, and M.Y. wrote the manuscript with B.Z. and Y.Z. providing theory support; K.W. and T.T. provided the hBN crystals.

COMPETING INTERESTS

The authors declare no competing interests.

ADDITIONAL INFORMATION

Correspondence and requests for materials should be addressed to Matthew Yankowitz.

DATA AVAILABILITY

Source data are available for this paper. All other data that support the findings of this study are available from the corresponding author upon request.

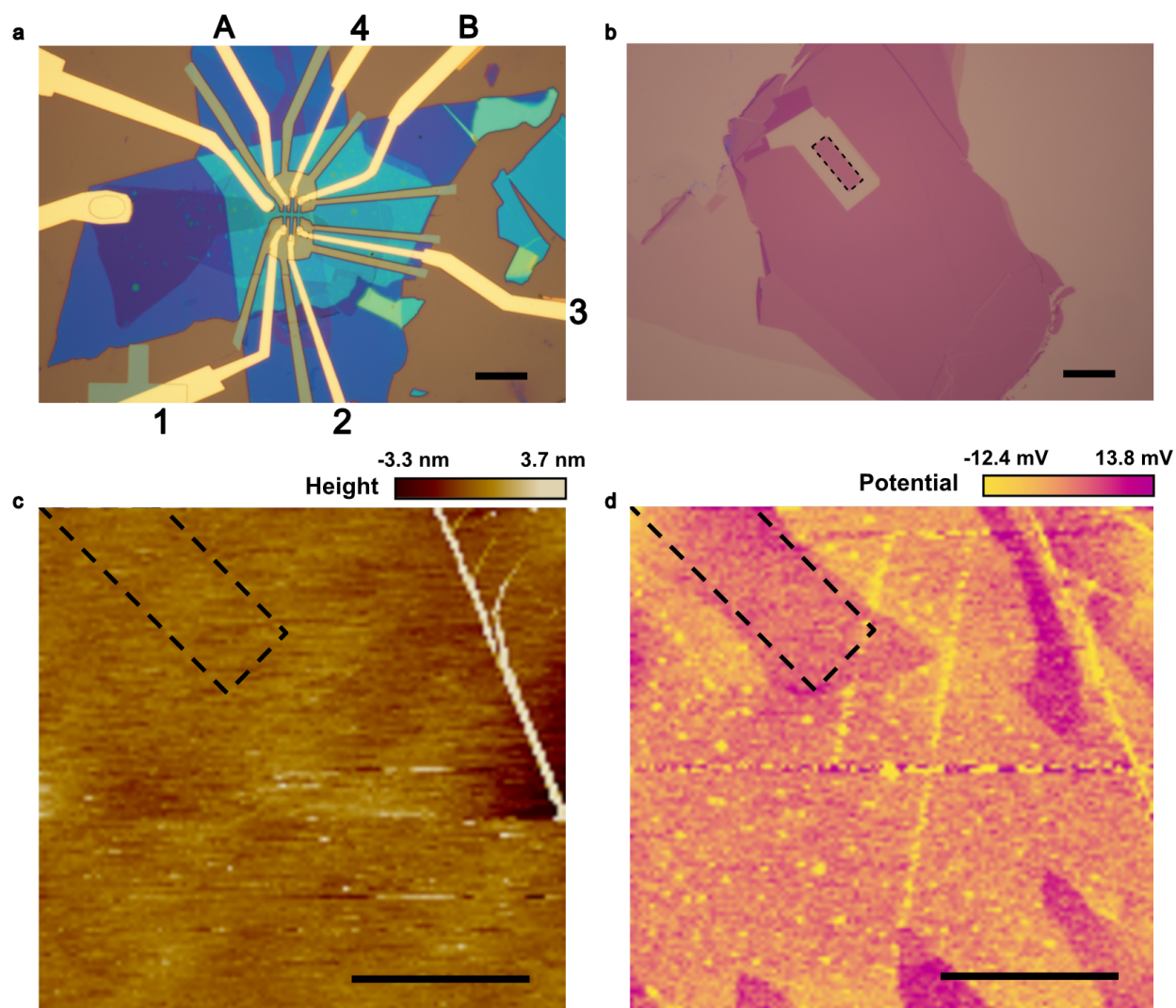
REFERENCES

- [1] Cai, J. *et al.* Signatures of fractional quantum anomalous Hall states in twisted MoTe_2 . *Nature* **622**, 63–68 (2023).
- [2] Zeng, Y. *et al.* Thermodynamic evidence of fractional Chern insulator in moiré MoTe_2 . *Nature* **622**, 69–73 (2023).

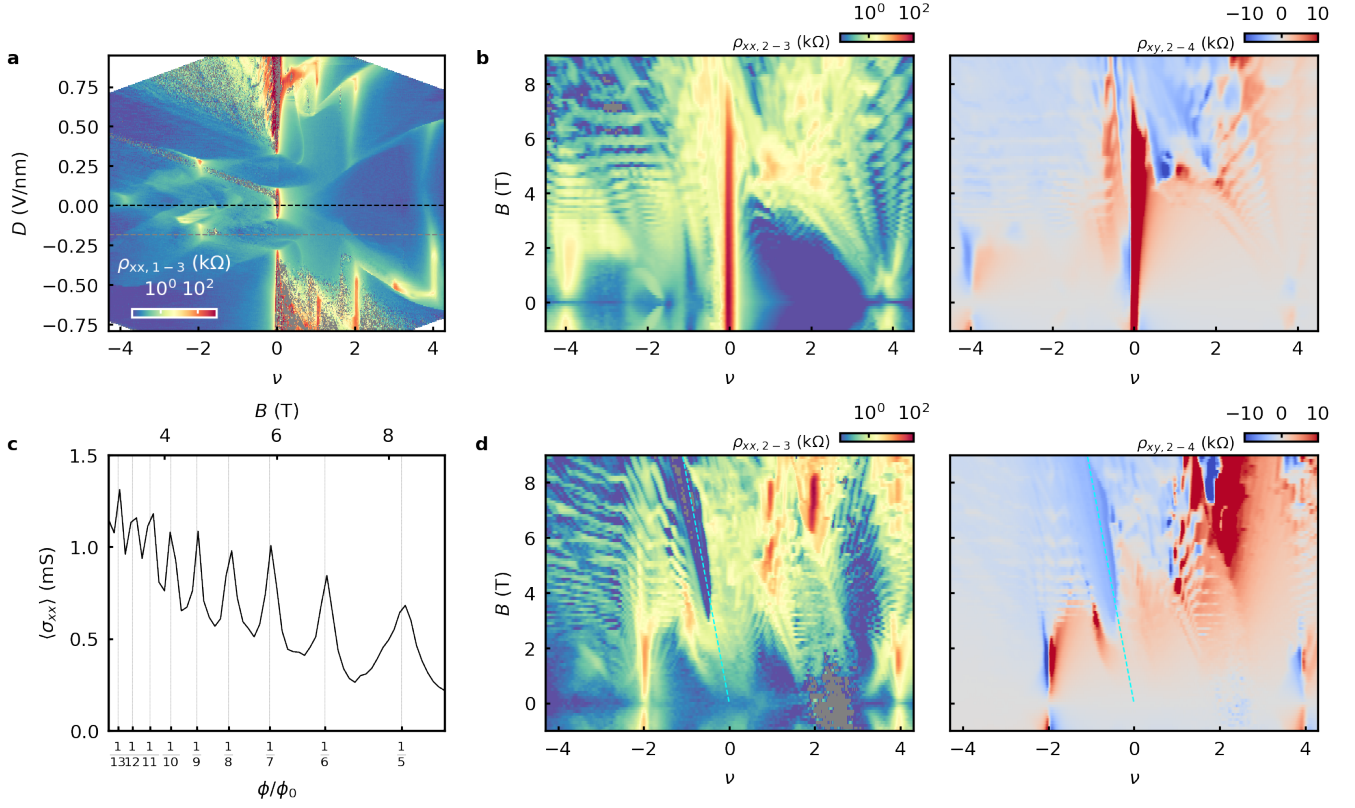
- [3] Park, H. *et al.* Observation of fractionally quantized anomalous Hall effect. *Nature* **622**, 74–79 (2023).
- [4] Xu, F. *et al.* Observation of integer and fractional quantum anomalous Hall effects in twisted bilayer MoTe₂. *Physical Review X* **13**, 031037 (2023).
- [5] Lu, Z. *et al.* Fractional quantum anomalous Hall effect in multilayer graphene. *Nature* **626**, 759–764 (2024).
- [6] Xie, J. *et al.* Even- and odd-denominator fractional quantum anomalous Hall effect in graphene moiré superlattices. *arXiv:2405.16944* (2024).
- [7] Goldman, H., Reddy, A. P., Paul, N. & Fu, L. Zero-field composite Fermi liquid in twisted semiconductor bilayers. *Physical Review Letters* **131**, 136501 (2023).
- [8] Dong, J., Wang, J., Ledwith, P., Vishwanath, A. & Parker, D. E. Composite Fermi liquid at zero magnetic field in twisted MoTe₂. *Physical Review Letters* **131**, 136502 (2023).
- [9] Reddy, A. P. & Fu, L. Toward a global phase diagram of the fractional quantum anomalous Hall effect. *arXiv:2308.10406* (2023).
- [10] Xu, C., Mao, N., Zeng, T. & Zhang, Y. Multiple Chern bands in twisted MoTe₂ and possible non-abelian states. *arXiv:2403.17003* (2024).
- [11] Wang, C. *et al.* Higher Landau-level analogues and signatures of non-abelian states in twisted bilayer MoTe₂. *arXiv:2404.05697* (2024).
- [12] Chen, F., W.-W., L., Zhu, W. & Sheng, D. N. Robust non-abelian even-denominator fractional Chern insulator in twisted bilayer MoTe₂. *arXiv:2405.08386* (2024).
- [13] Reddy, A. P., Paul, N., Abouelkomsan, A. & Fu, L. Non-abelian fractionalization in topological minibands. *arXiv:2403.00059* (2024).
- [14] Dong, Z., Patri, A. S. & Senthil, T. Theory of fractional quantum anomalous Hall phases in pentalayer rhombohedral graphene moiré structures. *arXiv:2311.03445* (2023).
- [15] Zhou, B., Yang, H. & Zhang, Y. Fractional quantum anomalous Hall effects in rhombohedral multilayer graphene in the moiréless limit and in Coulomb imprinted superlattice. *arXiv:2311.04217* (2023).
- [16] Dong, J. *et al.* Anomalous Hall crystals in rhombohedral multilayer graphene I: Interaction-driven Chern bands and fractional quantum Hall states at zero magnetic field. *arXiv:2311.05568* (2023).
- [17] Guo, Z., Lu, X. & Liu, J. Theory of fractional Chern insulator states in pentalayer graphene moiré superlattice. *arXiv:2311.14368* (2023).
- [18] Kwan, Y., Yu, J., Herzog-Arbeitman, J., Efetov, D. & Regnault, A., N. Bernevig. Moiré fractional Chern insulators III: Hartree-Fock phase diagram, magic angle regime for Chern insulator states, the role of the moiré potential and Goldstone gaps in rhombohedral graphene superlattices. *arXiv:2312.11617* (2023).
- [19] Sheng, D. N., Reddy, A. P., Abouelkomsan, A., Bergholtz, E. J. & Fu, L. Quantum anomalous Hall crystal at fractional filling of moiré superlattices. *Physical Review Letters* **133**, 066601 (2024).
- [20] Song, X.-Y., Jian, C.-M., Fu, L. & Xu, C. Intertwined fractional quantum anomalous Hall states and charge density waves. *Physical Review B* **109**, 115116 (2024).
- [21] Tan, T. & Devakul, T. Parent Berry curvature and the ideal anomalous Hall crystal. *arXiv:2403.04196* (2024).
- [22] Soejima, T. *et al.* Anomalous Hall crystals in rhombohedral multilayer graphene II: General mechanism and a minimal model. *arXiv:2403.05522* (2024).
- [23] Dong, Z., Patri, A. S. & Senthil, T. Stability of anomalous Hall crystals in multilayer rhombohedral graphene. *arXiv:2403.07873* (2024).
- [24] Shen, X. *et al.* Stabilizing fractional Chern insulators via exchange interaction in moiré systems. *arXiv:2405.12294* (2024).
- [25] Kudo, K., Nakai, R. & Nomura, K. Quantum anomalous, quantum spin, and quantum valley Hall effects in pentalayer rhombohedral graphene. *arXiv:2406.14354* (2024).
- [26] Zeng, Y., Guerci, D., Crepel, V., Millis, A. J. & Cano, J. Sublattice structure and topology in spontaneously crystallized electronic states. *Physical Review Letters* **132**, 236601 (2024).
- [27] Crépel, V. & Cano, J. Efficient prediction of superlattice and anomalous miniband topology from quantum geometry. *arXiv:2306.17843* (2024).
- [28] Yu, J., Herzog-Arbeitman, J., Kwan, Y. H., Regnault, N. & Bernevig, B. A. Moiré fractional Chern insulators IV: Fluctuation-driven collapse of FCIs in multi-band exact diagonalization calculations on rhombohedral graphene. *arXiv:2407.13770* (2024).
- [29] Huang, K., Das Sarma, S. & Li, X. Fractional quantum anomalous Hall effect in rhombohedral multilayer graphene with a strong displacement field. *arXiv:2408.05139* (2024).
- [30] Balents, L., Dean, C. R., Efetov, D. K. & Young, A. F. Superconductivity and strong correlations in moiré flat bands. *Nature Physics* **16**, 725–733 (2020).
- [31] Andrei, E. Y. & MacDonald, A. H. Graphene bilayers with a twist. *Nature Materials* **19**, 1265–1275 (2020).
- [32] Mak, K. F. & Shan, J. Semiconductor moiré materials. *Nature Nanotechnology* **17**, 686–695 (2022).
- [33] Nuckolls, K. P. & Yazdani, A. A microscopic perspective on moiré materials. *Nature Reviews Materials* **9**, 460–480 (2024).
- [34] Adak, P. C., Sinha, S., Agarwal, A. & Deshmukh, M. M. Tunable moiré materials for probing Berry physics and topology. *Nature Reviews Materials* **9**, 481–498 (2024).
- [35] Dean, C. R. *et al.* Hofstadter’s butterfly and the fractal quantum Hall effect in moiré superlattices. *Nature* **497**, 598–602 (2013).
- [36] Spanton, E. M. *et al.* Observation of fractional Chern insulators in a van der Waals heterostructure. *Science* **260**, 62–66 (2018).
- [37] Chen, G. *et al.* Tunable correlated Chern insulator and ferromagnetism in a moiré superlattice. *Nature* **579**, 56–61 (2020).
- [38] Xie, Y. *et al.* Fractional Chern insulators in magic-angle twisted bilayer graphene. *Nature* **600**, 439–443 (2021).
- [39] Polshyn, H. *et al.* Topological charge density waves at half-integer filling of a moiré superlattice. *Nature Physics* **18**, 42–47 (2022).
- [40] Su, R. *et al.* Generalized anomalous Hall crystals in twisted bilayer-trilayer graphene. *arXiv:2406.17766* (2024).
- [41] Streda, P. Quantised Hall effect in a two-dimensional periodic potential. *J. Phys. C* **15**, L1299 (1982).
- [42] Streda, P. Theory of quantised Hall conductivity in two dimensions. *J. Phys. C* **15**, L717 (1982).
- [43] Parameswaran, S. A. Anomalous Hall crystals or moiré Chern insulators? Spontaneous versus explicit translational symmetry breaking in graphene pentalayers. *DOI:10.36471/JCCM_January-2024_02* (2024).

- [44] Regan, E. C. *et al.* Mott and generalized Wigner crystal states in WSe_2/WS_2 moiré superlattices. *Nature* **579**, 359–363 (2020).
- [45] Polshyn, H. *et al.* Electrical switching of magnetic order in an orbital Chern insulator. *Nature* **588**, 66–70 (2020).
- [46] Grover, S. *et al.* Chern mosaic and Berry-curvature magnetism in magic-angle graphene. *Nature Physics* **18**, 885–892 (2022).
- [47] Kolář, K., Zhang, Y., Nadj-Perge, S., von Oppen, F. & Lewandowski, C. Electrostatic fate of N -layer moiré graphene. *Phys. Rev. B* **108**, 195148 (2023).
- [48] Liu, X. *et al.* Tuning electron correlation in magic-angle twisted bilayer graphene using Coulomb screening. *Science* **271**, 1261–1265 (2021).
- [49] Han, T. *et al.* Orbital multiferroicity in pentalayer rhombohedral graphene. *Nature* **623**, 41–47 (2023).
- [50] Han, T. *et al.* Correlated insulator and Chern insulators in pentalayer rhombohedral-stacked graphene. *Nature Nanotechnology* **19**, 181–187 (2024).
- [51] Li, H. *et al.* Electrode-free anodic oxidation nanolithography of low-dimensional materials. *Nano Letters* **18**, 8011–8015 (2018).
- [52] Zhou, H. *et al.* Half- and quarter-metals in rhombohedral trilayer graphene. *Nature* **598**, 429–433 (2021).
- [53] Shi, Y. *et al.* Electronic phase separation in multilayer rhombohedral graphite. *Nature* **584**, 210–214 (2020).
- [54] Zhang, F., Jung, J., Fiete, G. A., Niu, Q. & MacDonald, A. H. Spontaneous quantum Hall states in chirally stacked few-layer graphene systems. *Phys. Rev. Lett.* **106**, 156801 (2011).
- [55] Velasco, J. *et al.* Transport spectroscopy of symmetry-broken insulating states in bilayer graphene. *Nature Nanotechnology* **7**, 156–160 (2012).
- [56] Weitz, R. T., Allen, M. T., Feldman, B. E., Martin, J. & Yacoby, A. Broken-symmetry states in doubly gated suspended bilayer graphene. *Science* **330**, 812–816 (2010).
- [57] Liu, K. *et al.* Spontaneous broken-symmetry insulator and metals in tetralayer rhombohedral graphene. *Nature Nanotechnology* **19**, 188–195 (2024).
- [58] Sha, Y. *et al.* Observation of a Chern insulator in crystalline ABCA-tetralayer graphene with spin-orbit coupling. *Science* **384**, 414–419 (2024).
- [59] Song, J. C. W. & Vignale, G. Hall diffusion anomaly and transverse Einstein relation. *arXiv:2007.10373* (2020).
- [60] Zhu, J., Li, T., Young, A. F., Shan, J. & Mak, K. F. Quantum oscillations in two-dimensional insulators induced by graphite gates. *Phys. Rev. Lett.* **127**, 247702 (2021).
- [61] Park, Y., Kim, Y., Chittari, B. L. & Jung, J. Topological flat bands in rhombohedral tetralayer and multilayer graphene on hexagonal boron nitride moiré superlattices. *Phys. Rev. B* **108**, 155406 (2023).
- [62] Fukui, T., Hatsugai, Y. & Suzuki, H. Chern numbers in discretized Brillouin zone: efficient method of computing (spin) Hall conductances. *Journal of the Physical Society of Japan* **74**, 1674–1677 (2005).

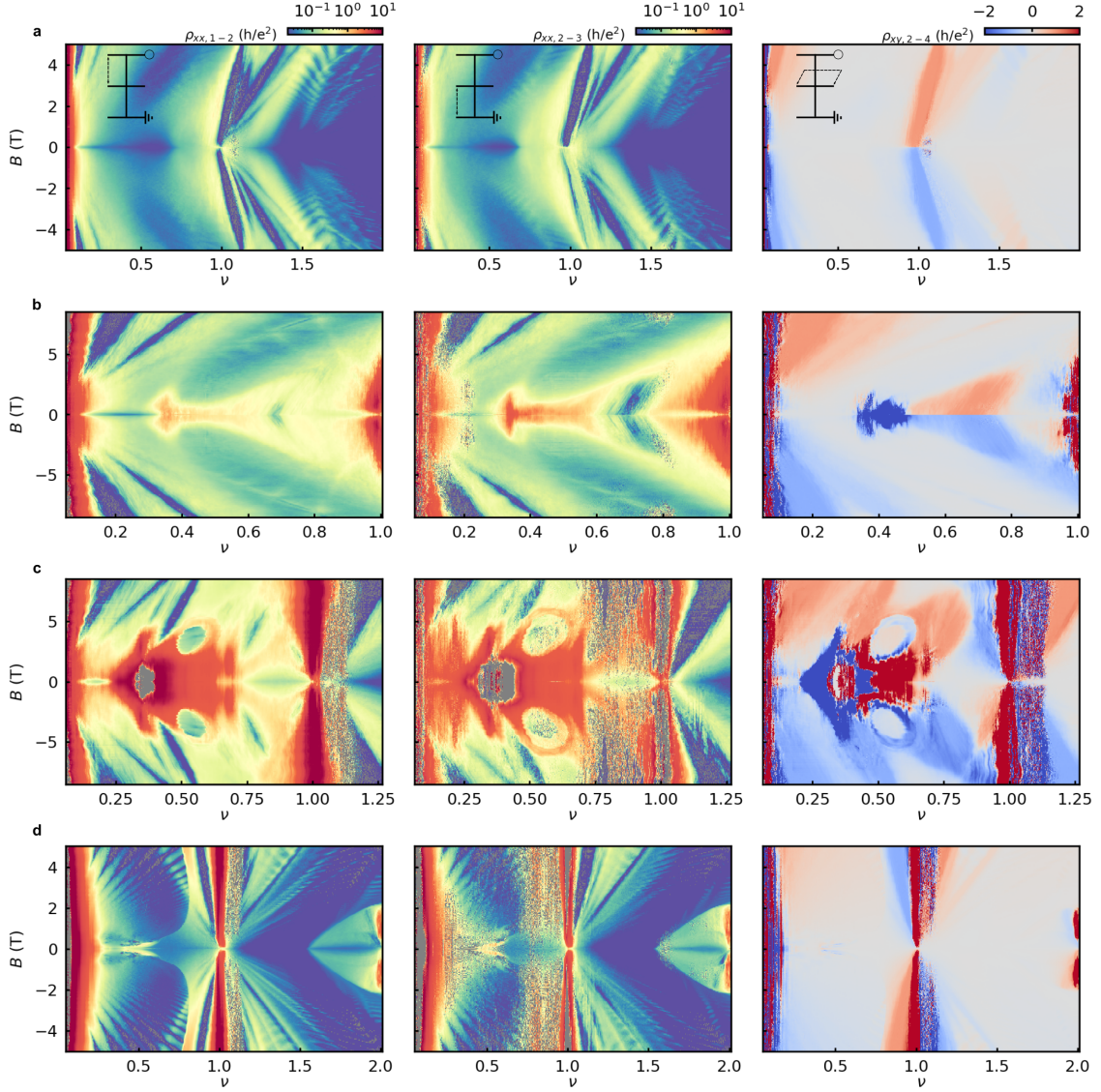
EXTENDED DATA



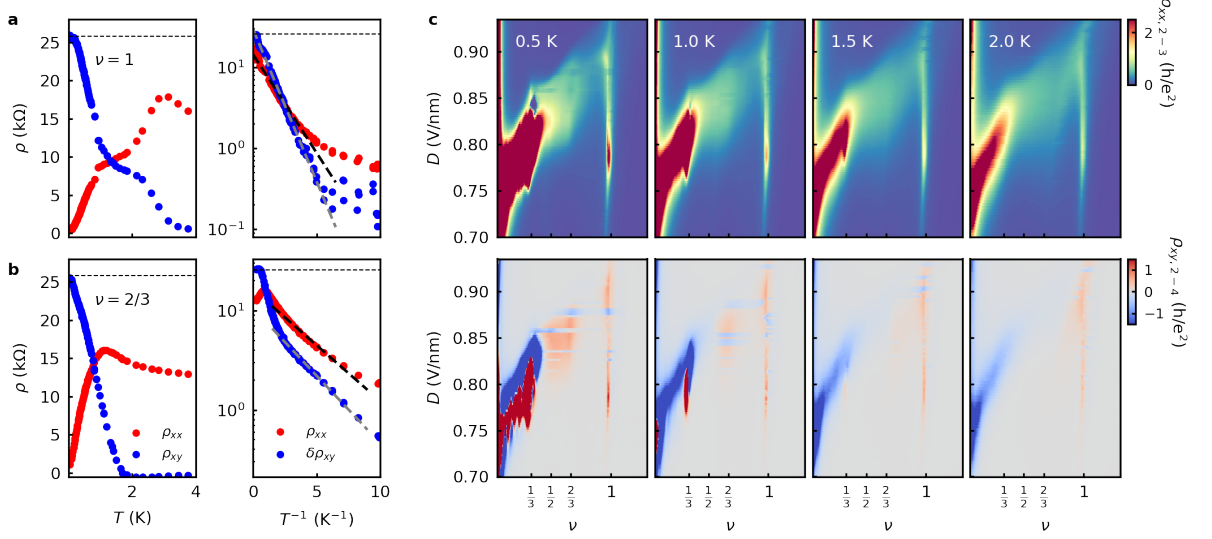
Extended Data Fig. 1. **Device image and fabrication.** **a**, Optical micrograph of the device. Electrical contacts are labeled A-B and 1-4. **b**, Optical micrograph of the pentalayer graphene flake after performing anodic oxidation nanolithography to isolate a rhombohedral domain (outlined by the black dashed rectangle). **c**, AFM topograph of the pentalayer flake taken around the area where the anodic oxidation nanolithography was performed (black dashed rectangle). **d**, AM-KPFM measurement of same area as in **c**. The rhombohedral domain is identified as described in the Methods and in Supplementary Information Fig. S1. All scale bars are 10 μm .



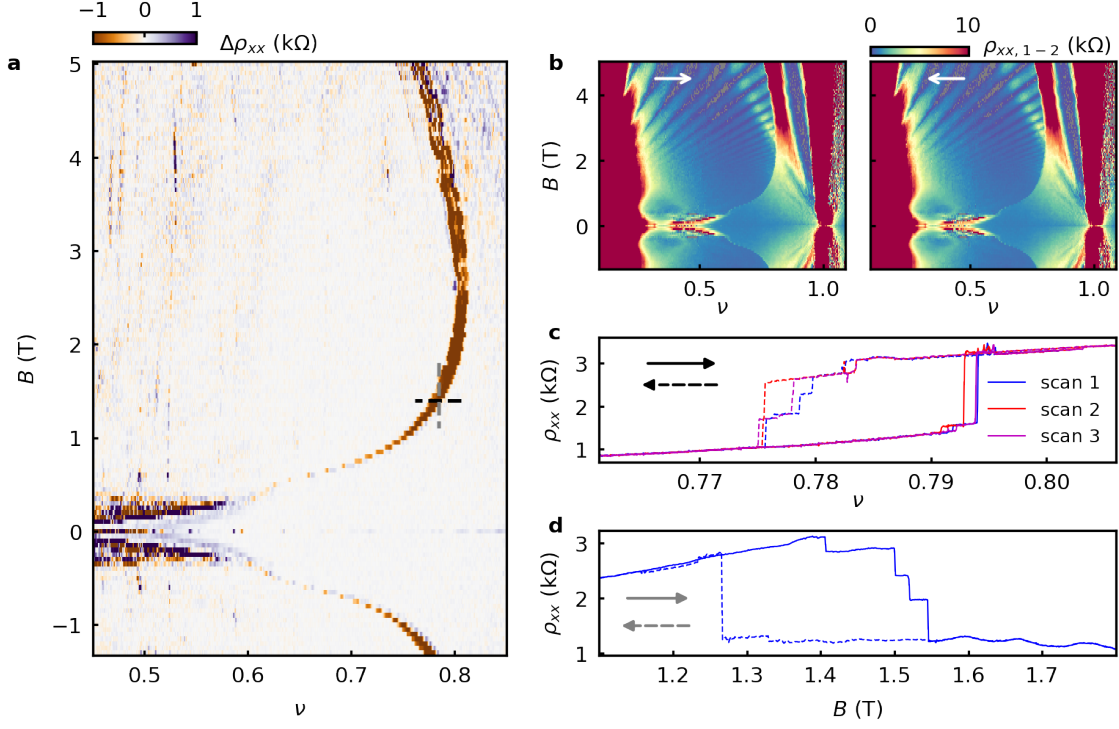
Extended Data Fig. 2. **Landau fan characterization.** **a**, Map of ρ_{xx} at $B = 0$ reproduced from Fig. 1b, with dashed black and gray lines denoting where the Landau fans in **b** and **d** are acquired. **b**, Landau fan of ρ_{xx} and ρ_{xy} acquired at $D = 0$ (black line in **a**). **c**, Averaged conductance, $\langle\sigma_{xx}\rangle = \rho_{xx}/(\rho_{xx}^2 + \rho_{xy}^2)$ calculated from the Landau fan in **b** across all accessible n as a function of B . Brown-Zak oscillations occur when $\phi/\phi_0 = 4B/n_s\phi_0 = p/q$, where p and q are integers. The best fit to the data yields $n_s = 3.98 \times 10^{12} \text{ cm}^{-2}$ (see Methods). **d**, Landau fan taken at $D = -0.185 \text{ V/nm}$ (gray line in **a**). The blue dashed line denotes a Streda slope of $C = -5$, confirming the sample is rhombohedral pentalayer graphene [50]. Data in **b-d** are taken with 1 nA bias current and are not (anti-)symmetrized.



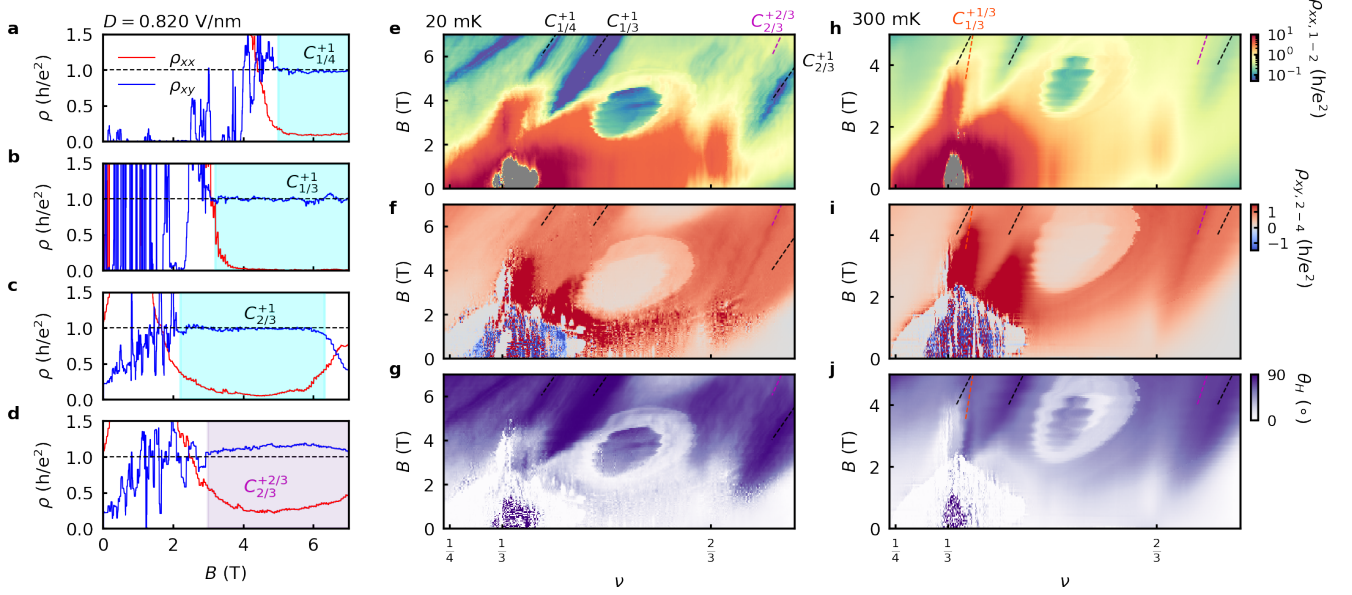
Extended Data Fig. 3. **Contact pair variation and unsymmetrized Landau fans.** Raw data (i.e., without symmetrization and antisymmetrization) for the Landau fans taken with different contact pairs at **a**, $D = 0.91$ V/nm, **b**, $D = 0.8625$ V/nm, **c**, $D = 0.826$ V/nm, and **d**, $D = 0.740$ V/nm. Schematics in **a** denote which contact pairs were used for the measurements, where current was sourced at the top right (circle) and drained to the bottom right (ground) and the potential difference was measured between the contact pairs denoted by the dashed black arrows. The device had two ρ_{xx} contact pairs (leftmost and center plots, using the same color scale) and one ρ_{xy} contact pair (rightmost plots). The two ρ_{xx} contact pairs are very similar overall, although exhibit small differences in the detailed features of states indicating slight sample inhomogeneity. All three contact pairs exhibit vertical strips where the data appears “speckled”; these are artifacts resulting from poor contact equilibration for certain ranges of ν . We were unable to eliminate these artifacts using the silicon gate voltage.



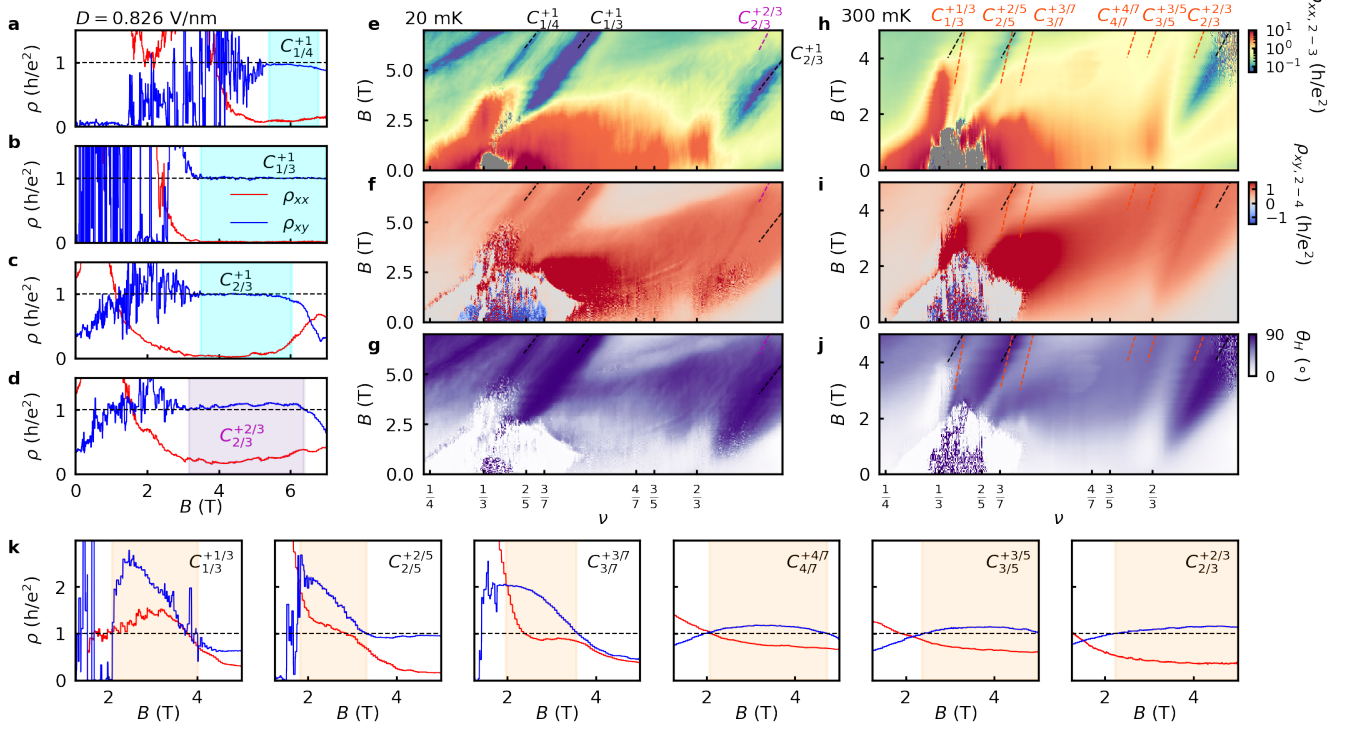
Extended Data Fig. 4. **Temperature dependence of the correlated states at $0 < \nu \lesssim 1$.** **a**, ρ_{xx} and ρ_{xy} measured as a function of temperature at $\nu = 1$ and $D = 0.909$ V/nm. Dashed black lines indicate $\rho = h/e^2$. The right panel is shown as an Arrhenius plot, from which we extract gap sizes based on the slopes in the thermally activated regime. Here, $\delta\rho_{xy} = \rho_{xy}[T = 20 \text{ mK}] - \rho_{xy}$. The dashed black line is the fit to the ρ_{xx} curve, assuming $\rho_{xx} \propto \exp(-\Delta/2k_B T)$, and yields $\Delta_{\nu=1}^{xx} = 0.096 \pm 0.001$ meV. The dashed gray line is a fit to the $\delta\rho_{xy}$ curve, which yields $\Delta_{\nu=1}^{xy} = 0.149 \pm 0.001$ meV. **b**, Similar plots for the $\nu = 2/3$ state at $D = 0.870$ V/nm. Here, the gap size is determined to be $\Delta_{\nu=2/3}^{xx} = 0.044 \pm 0.001$ meV and $\Delta_{\nu=2/3}^{xy} = 0.054 \pm 0.001$ meV. **c**, ρ_{xx} and ρ_{xy} maps at $B = 0$ in 0.5 K increments, as indicated in the top panel. Data taken with $I_{ac} = 14$ pA in **a-b** and $I_{ac} = 1$ nA in **c**.



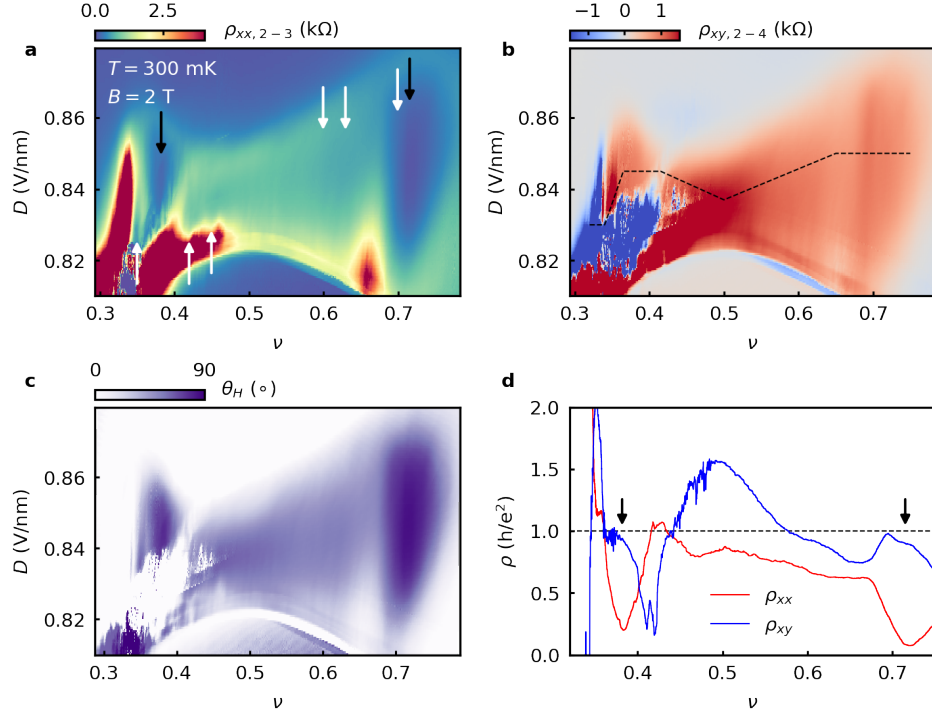
Extended Data Fig. 5. **Hysteresis across the sharp curved feature in the $D = 0.740$ V/nm Landau fan.** **a**, Map of the difference between the resistance measured upon sweeping the doping back and forth as a function of magnetic field, $\Delta\rho_{xx}$. There is substantial hysteresis along a curved trajectory matching the abrupt phase transition in the Landau fan in Fig. 2b, indicating that it is a first-order phase transition. As argued in the text, the right-hand side of the phase transition appears to be a state with electronic crystalline order, whereas the left-hand side appears to correspond to a state without spontaneous translational symmetry breaking. **b**, Raw data of the Landau fans acquired with each sweeping direction used to construct the map in **a**. **c**, Three consecutive measurements (scans 1-3) of ρ_{xx} taken as the doping is swept back and forth at fixed B denoted by the horizontal black dashed line in **a**. The hysteresis with doping and non-reproducibility upon repeated scanning are all indications of the first-order phase transition. **d**, A similar measurement at fixed ν but instead sweeping B back and forth, taken along the path indicated by the vertical gray dashed line in **a**. The measurement also exhibits substantial hysteresis.



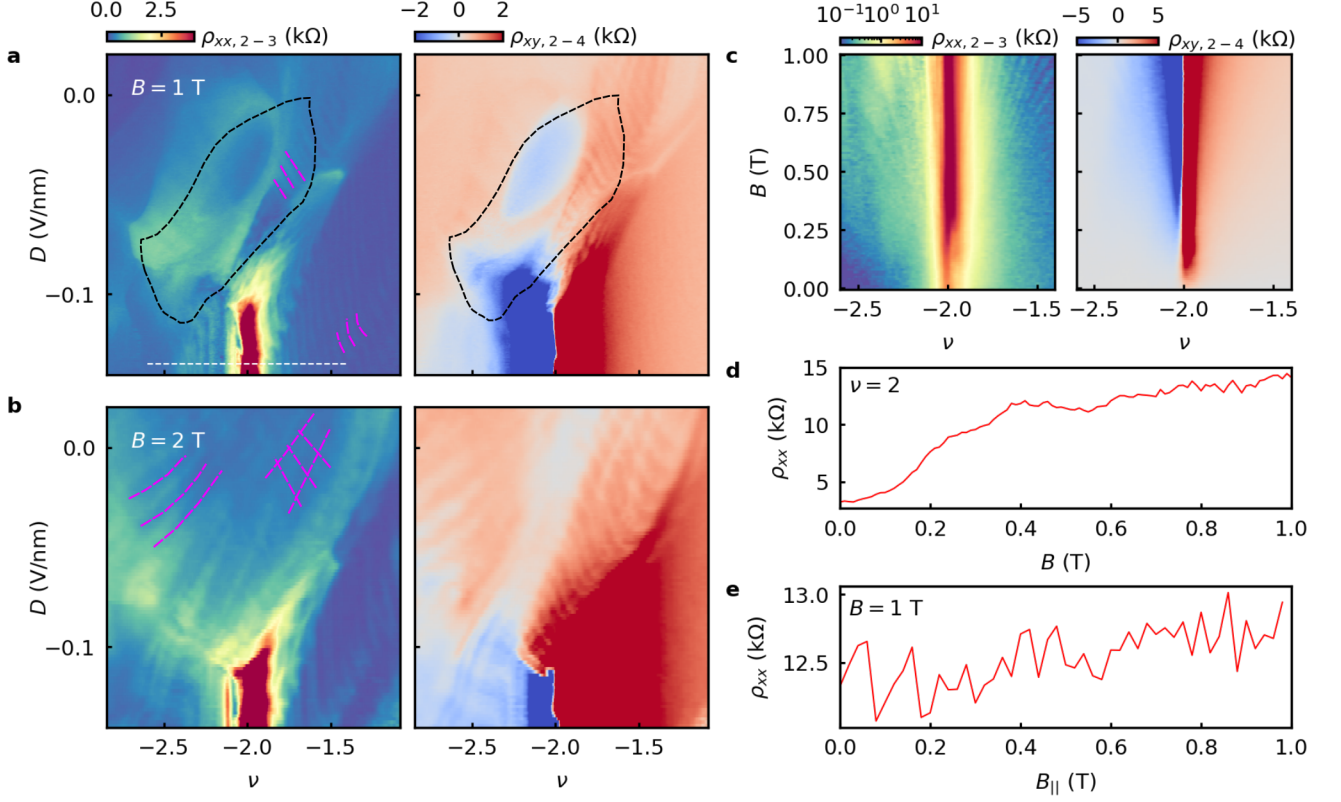
Extended Data Fig. 6. **Line cuts and temperature dependence of the $D = 0.820$ V/nm Landau fan.** **a**, Line traces of ρ_{xx} and ρ_{xy} taken along the trajectory indicated by the black dashed line associated with the $C_{1/4}^{+1}$ state in **e**. **b**, Same for the $C_{1/3}^{+1}$ state. **c**, Same for the $C_{2/3}^{+1}$ state. **d**, Same for the $C_{2/3}^{+2/3}$ state corresponding to the trajectory indicated by the purple dashed line in **e**. **e**, Landau fan of ρ_{xx} acquired at 20 mK. **f**, Same for ρ_{xy} . Note that **c-f** are reproduced from Fig. 3 for completeness. **g**, Landau fan showing the Hall angle, θ_H . Regions of darkest purple are consistent with Chern insulators. **h-j**, Similar measurements as in **e-g** but at 300 mK and shown over a slightly different range of B and ν . The orange dashed line marks the trajectory of a $C_{1/3}^{+1/3}$ FCI state. There is a simultaneous dip in ρ_{xx} , a large enhancement of ρ_{xy} , and a large enhancement of θ_H over an intermediate range of magnetic field ($2 \text{ T} \lesssim B \lesssim 4 \text{ T}$) in these measurements, potentially indicating an incipient in-field FCI state corresponding to $\nu = 1/3$.



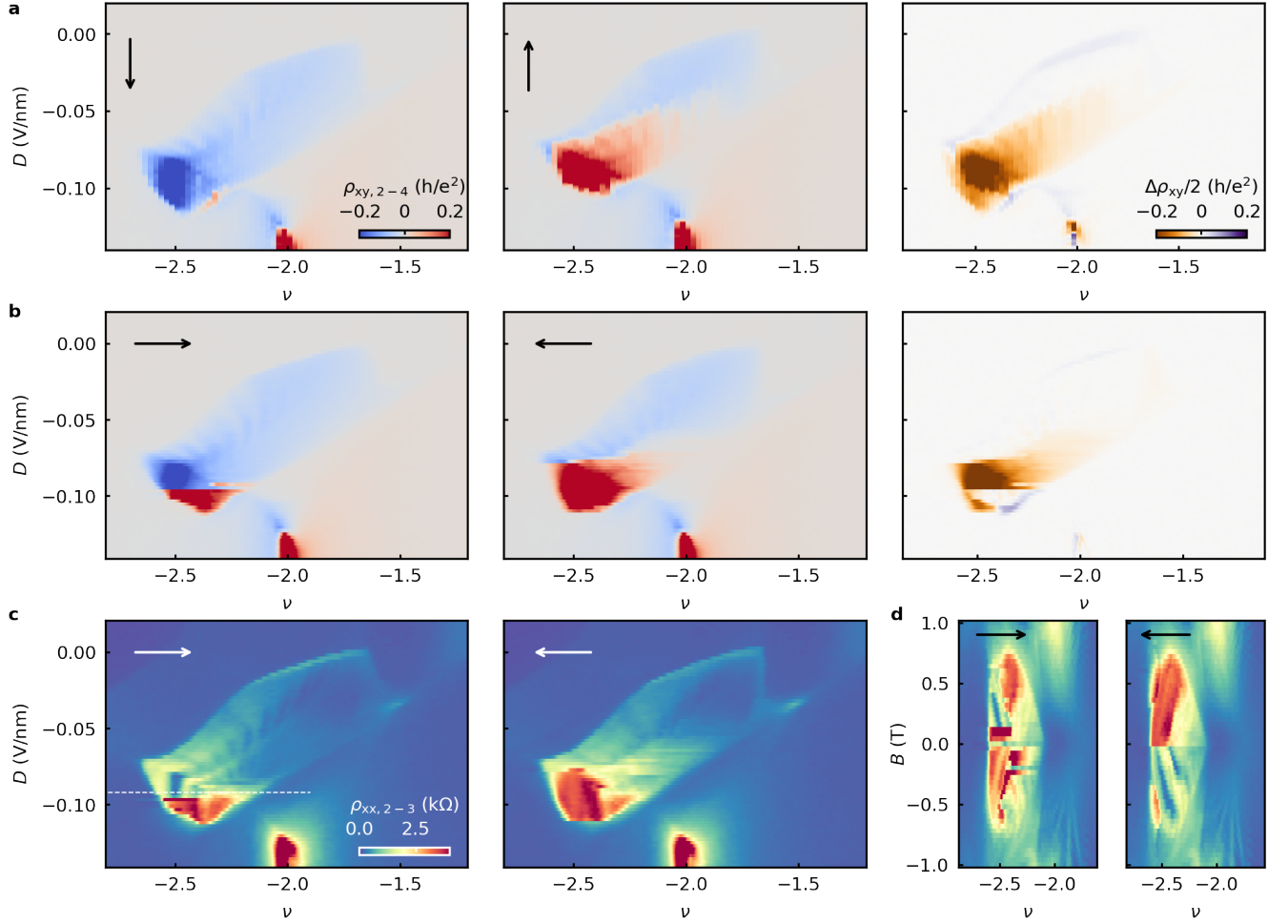
Extended Data Fig. 7. **Line cuts and temperature dependence of a $D = 0.826$ V/nm Landau fan.** **a-j**, Same plots for the Landau fan taken at a value of D that is only 6 mV/nm larger than in Extended Data Fig. 6. Despite this small difference, a number of features change. Perhaps most notably, the oval near $\nu \approx 0.6$ in which there is a first-order phase transition to a different state is gone (except for a weak hint of its recurrence in the fan at 300 mK). Additionally, the 300 mK fan has additional faint features possibly indicating other in-field FCI states. There are enhanced regions of θ_H for $2 \text{ T} \lesssim B \lesssim 3 \text{ T}$ consistent with the anticipated slopes of FCI states corresponding to $\nu = 2/5$ and $3/7$. There is also a weak feature for $2 \text{ T} \lesssim B \lesssim 5 \text{ T}$ along the trajectory of an FCI state corresponding to $\nu = 3/5$. **k** Line traces of ρ_{xx} and ρ_{xy} at $T = 300$ mK taken along the trajectories of all the Jain-sequence states up to denominator of 7. The orange shaded regions correspond to contiguous regions satisfying both $\rho_{xy} > h/e^2$ and $\rho_{xy} > \rho_{xx}$. We stress that these observations alone do not prove the existence of these additional Jain-sequence in-field FCI states, but motivate their possible emergence.



Extended Data Fig. 8. **Intermixed FCI and TEC states at $B = 2$ T.** **a**, Map of ρ_{xx} symmetrized at $|B| = 2$ T and $T = 300$ mK. The black arrows indicate the anticipated positions of $C = +1$ states originating from $\nu = 1/3$ and $2/3$, based on their evolution in B as described by the Streda formula. The white arrows correspond to the anticipated positions of Jain-sequence FCI states, from left to right: $\nu = 1/3, 2/5, 3/7, 4/7, 3/5, 2/3$. These markers are shown only to indicate the anticipated positions of these states, and do not necessarily imply that there are features there (although in many cases there do appear to be). **b**, Antisymmetrized map of ρ_{xy} . The curved feature at the bottom of the maps marks the first-order phase transition analyzed in Extended Data Fig. 5. **c**, Map of θ_H . **d**, Line traces of ρ_{xx} and ρ_{xy} taken along the black dashed path shown in **b**. The black arrows denote the positions of the $C_{1/3}^{+1}$ (left) and $C_{2/3}^{+1}$ (right) states based upon their evolution described by the Streda formula. Nearby these positions, $\rho_{xy} \approx h/e^2$ and there is a deep suppression of ρ_{xx} , consistent with the $C = +1$ Chern insulators analyzed in the main text. In between, there is a wide range of fractional ν where the antisymmetrized ρ_{xy} far exceeds h/e^2 . Although there is also a very large ρ_{xx} approaching h/e^2 , there is nevertheless a large Hall angle. Together with the analysis of the Landau fans in Extended Data Figs. 6 and 7, this behavior is possibly consistent with in-field FCI states. The large ρ_{xx} has been seen in other FCI states reported in Refs. 5 and 6.



Extended Data Fig. 9. **Multiband transport and correlated insulator near $\nu = -2$.** **a**, Maps of ρ_{xx} (left) and ρ_{xy} (right) taken at $B = 1$ T. The black dashed enclosure denotes the boundaries of the valley-polarized pocket at $B = 0$ (corresponding to the condition of $\rho_{xy} = 0$). In general, quantum oscillations do not remain at fixed values of ν as D is changed (selected examples are denoted by the dashed purple curves). Such behavior indicates that these states originate from a Fermi surface with multiple coexisting pockets. **b**, The same maps from **a**, taken at $B = 2$ T. The valley-polarized pocket is completely gone at this magnetic field. There are crisscrossing quantum oscillations within the region of $n - D$ occupied by the valley-polarized pocket at $B = 0$, suggesting that this pocket arises out of a Fermi surface with multiple pockets. **c**, Landau fan of ρ_{xx} (left) and ρ_{xy} (right) taken at $D = -0.135$ V/nm (dashed white line in **a**). The primary state is a trivial $C = 0$ insulator at $\nu = -2$, consistent with a spin-polarized insulator. **d**, ρ_{xx} measured as a function of B at $\nu = 2$. **e**, The same measurement performed at $B = 1$ T as a function of in-plane magnetic field, $B_{||}$. All data taken with 1 nA bias current.



Extended Data Fig. 10. **Hysteresis of the orbital magnetic state and incipient Chern insulators near $\nu = -2$.** **a**, Map of ρ_{xy} showing the hole-doped valley-polarized pocket, acquired by sweeping D down (left) and up (middle) as the fast axis with ν as the slow axis. (right) Difference between the down and up sweeps, $\Delta\rho_{xy}/2$. **b**, Same as **a**, but with ν as the fast axis and D the slow axis. **c**, ρ_{xx} maps corresponding to those shown in **b**. Data in **a-c** were taken at $B = 0.2$ T (not symmetrized). **d**, Landau fans taken along the white dashed line in **c**, sweeping the density axis forward and backward. The sign of the slopes of the most prominent Chern states switch upon changing the sweeping direction, reflecting the flipping sign of the orbital magnetism. All data taken with 1 nA bias current.

Supplementary Information: Interplay of electronic crystals with integer and fractional Chern insulators in moiré pentalayer graphene

Dacen Waters^{1,2*}, Anna Okounkova^{1*}, Ruiheng Su^{3,4}, Boran Zhou⁵, Jiang Yao¹, Kenji Watanabe⁶, Takashi Taniguchi⁷, Xiaodong Xu^{1,8}, Ya-Hui Zhang⁵, Joshua Folk^{3,4}, and Matthew Yankowitz^{1,8†}

¹*Department of Physics, University of Washington, Seattle, Washington, 98195, USA*

²*Intelligence Community Postdoctoral Research Fellowship Program,*

University of Washington, Seattle, Washington, 98195, USA

³*Quantum Matter Institute, University of British Columbia, Vancouver, British Columbia, V6T 1Z1, Canada*

⁴*Department of Physics and Astronomy, University of British Columbia, Vancouver, British Columbia, V6T 1Z1, Canada*

⁵*Department of Physics and Astronomy, Johns Hopkins University, Baltimore, Maryland, 21205, USA*

⁶*Research Center for Electronic and Optical Materials, National Institute for Materials Science, 1-1 Namiki, Tsukuba 305-0044, Japan*

⁷*Research Center for Materials Nanoarchitectonics, National Institute for Materials Science, 1-1 Namiki, Tsukuba 305-0044, Japan*

⁸*Department of Materials Science and Engineering, University of Washington, Seattle, Washington, 98195, USA*

**These authors contributed equally to this work. and*

†myank@uw.edu (M.Y.)

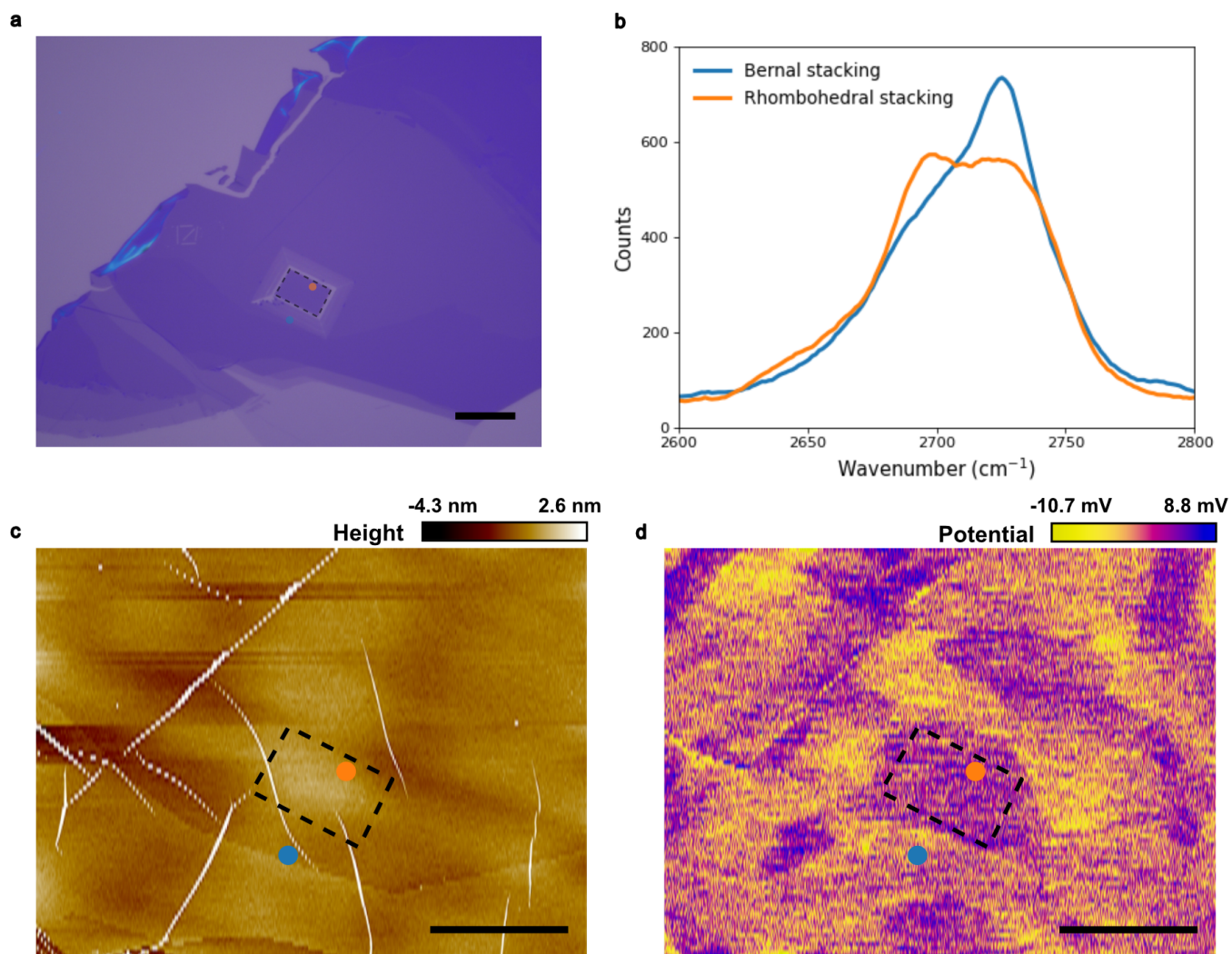


FIG. S1. **Characterization and isolation of rhombohedral domains using AFM and Raman spectroscopy.** **a**, Optical micrograph of a pentalayer graphene flake with a region of anodic oxidation nanolithography etching outlined by the black dashed box. The blue and orange dots correspond to locations where Raman spectroscopy was performed. **b**, Raman spectra corresponding to the positions denoted in **a**. **c**, AFM topograph of the pentalayer graphene flake (before etching), with the same black box and blue/orange markers as in **a**. **d**, AM-KPFM scan of same area as in **c**. Scale bars in **a**, **c**, and **d** are all $10\ \mu\text{m}$.

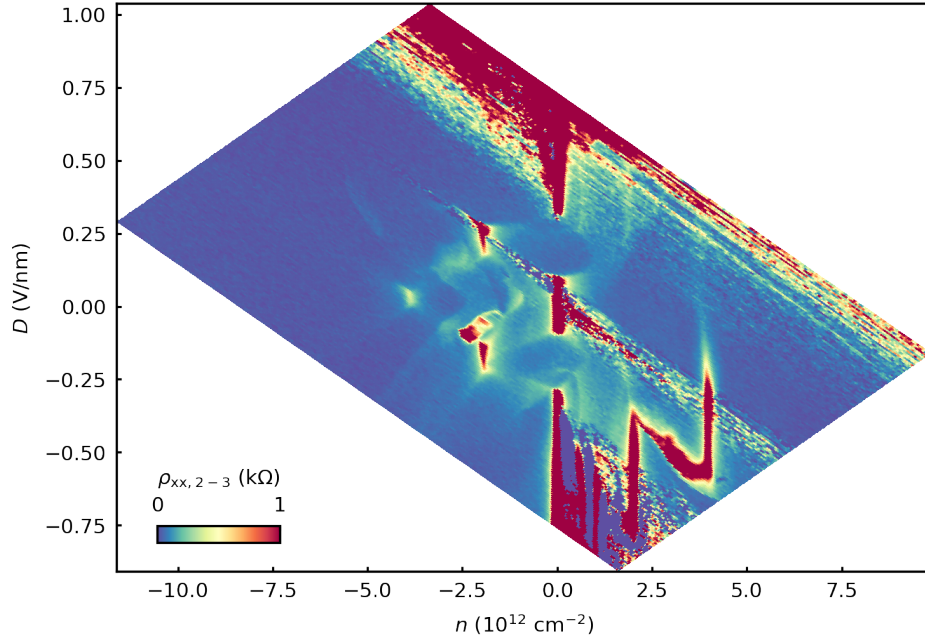


FIG. S2. **Large density range transport map.** Map of ρ_{xx} taken to the largest experimentally accessible value of n . Besides those analyzed in the main text, we observe no additional superlattice features out to $|n| = 11.59 \times 10^{12} \text{ cm}^{-2}$. This sets an upper limit on a secondary moiré wavelength from the misaligned hBN of 6.31 nm. Assuming a lattice mismatch of 1.7%, this corresponds to a lower limit on the twist angle of the misaligned hBN of 2.03° . The streaking on the upper right hand side of the map is a contact issue, which we can tune away using an appropriate value of the silicon gate voltage. Data taken with $I_{ac} = 1 \text{ nA}$.

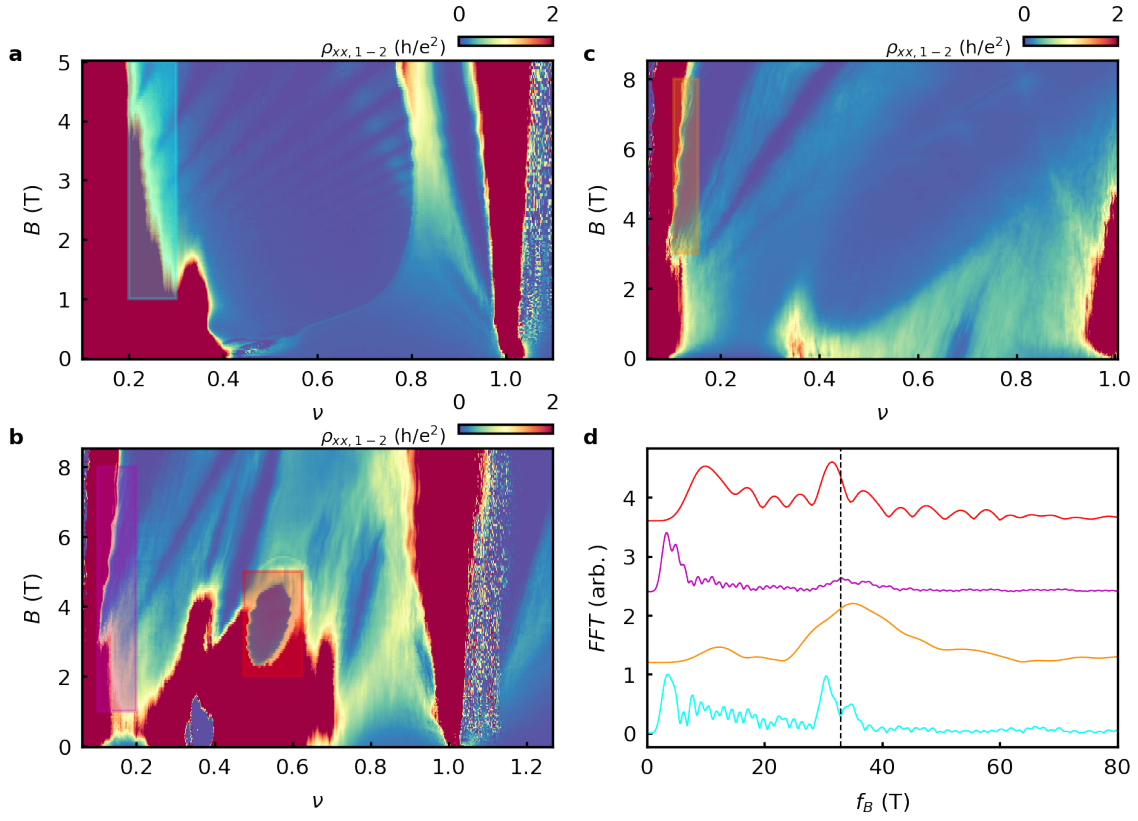


FIG. S3. **Gate-induced quantum oscillations.** Landau fan diagrams taken at **a**, $D = 0.768$ V/nm, **b**, $D = 0.863$ V/nm, and **c**, $D = 0.82$ V/nm. All of these exhibit oscillation features at constant values of B extending over a wide range of doping. **d**, Fast Fourier transform (FFT) of the ρ_{xx} signal with respect to B . Each curve is taken in the corresponding colored box in panels **a-c**. The curves are offset for clarity. Each exhibits a bump above the background at $f_B \approx 33$ T (dashed black line), although the signal varies substantially depending on the precise values of ν and D . This behavior is similar to that reported in Ref. [1] for regions with large dR/dn , indicating that the oscillations are features associated with one of the graphite gates rather than intrinsic to the physics of the moiré RPG.

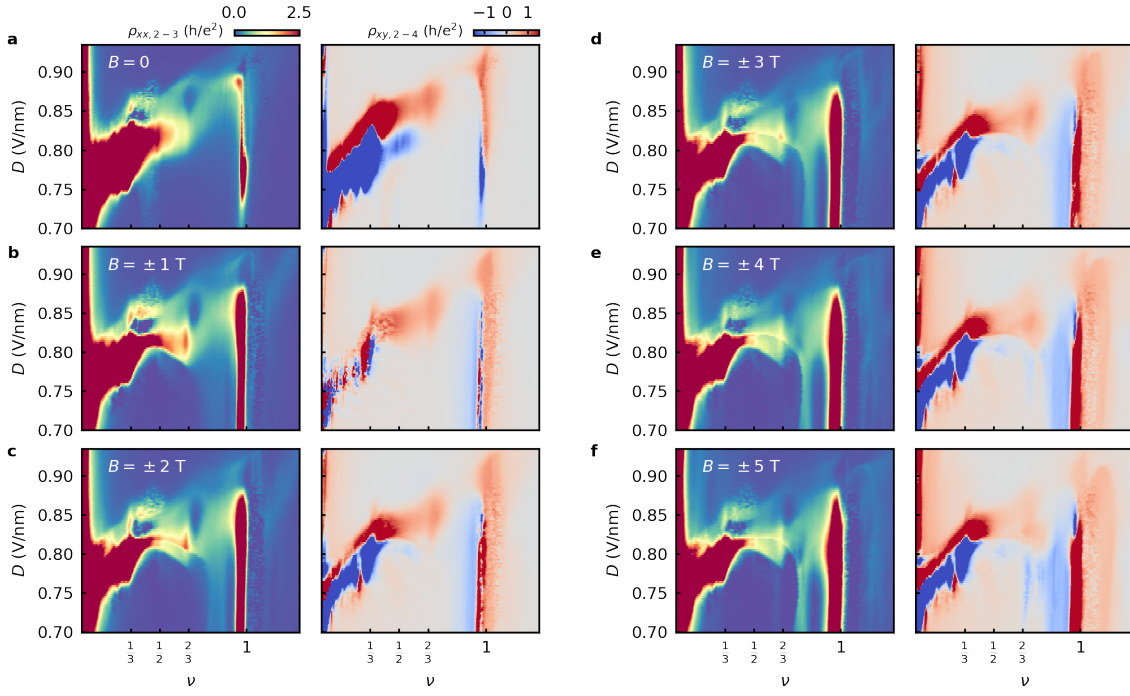


FIG. S4. **Magnetic field evolution of the high D region.** **a**, Maps of ρ_{xx} (left) and ρ_{xy} (right) with $B = 0$ up to 5 T. All measurements are taken with $I_{ac} = 1$ nA.

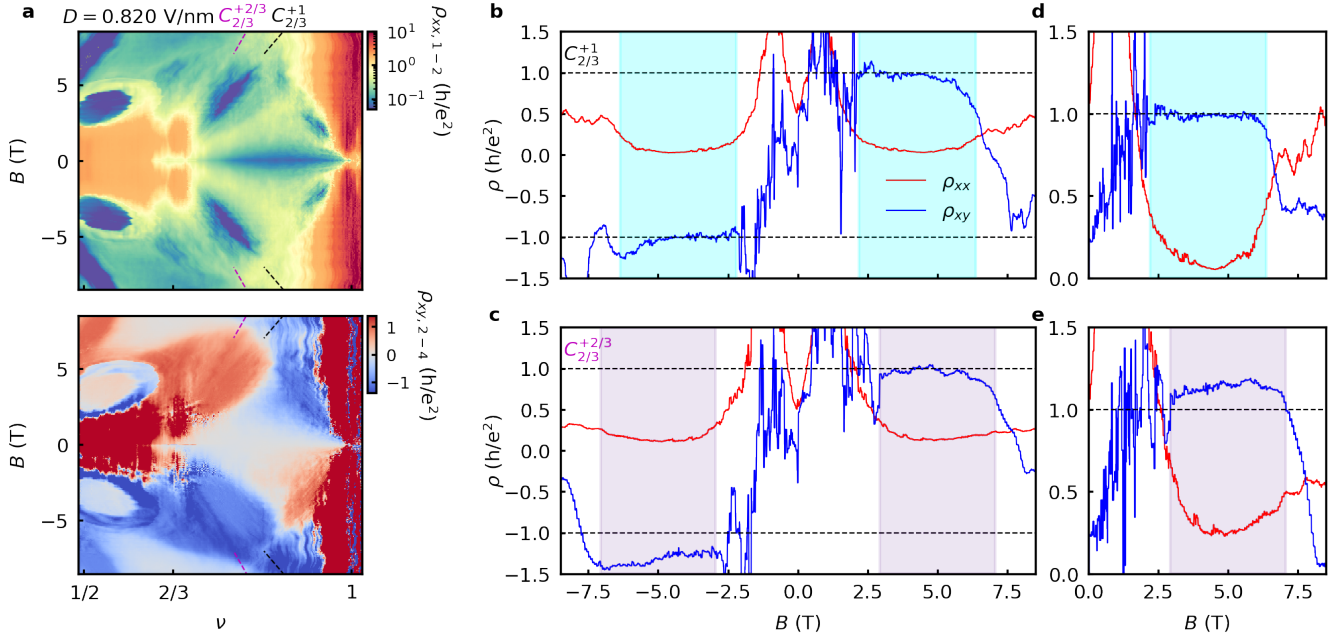


FIG. S5. **Line cuts from unsymmetrized Landau fans.** **a**, Landau fan at $D = 0.820$ V/nm showing ρ_{xx} without symmetrization (top) and ρ_{xy} without antisymmetrization (bottom). **b**, Line cuts along the trajectory of the $C_{2/3}^{+1}$ state. The cyan shaded region is the same magnetic field region identified from the symmetrized data in Fig. 3e (reproduced in **d**). **c**, Same as **a**, but for the $C_{2/3}^{+2/3}$ state. The purple shaded region is the same magnetic field region identified from the symmetrized data in Fig. 3f (reproduced in **e**). We find that there is a significant asymmetry of ρ_{xy} between the positive and negative field values. ρ_{xy} rarely exceeds h/e^2 for $B > 0$, but approaches the anticipated quantized value of $-3h/2e^2$ for $B < 0$. **d**, (Anti-)symmetrized curves for comparison with **b**. **e**, (Anti-)symmetrized curves for comparison with **c**. Because of the non-vanishing ρ_{xx} , antisymmetrization is evidently critical for properly assessing the value of ρ_{xy} .

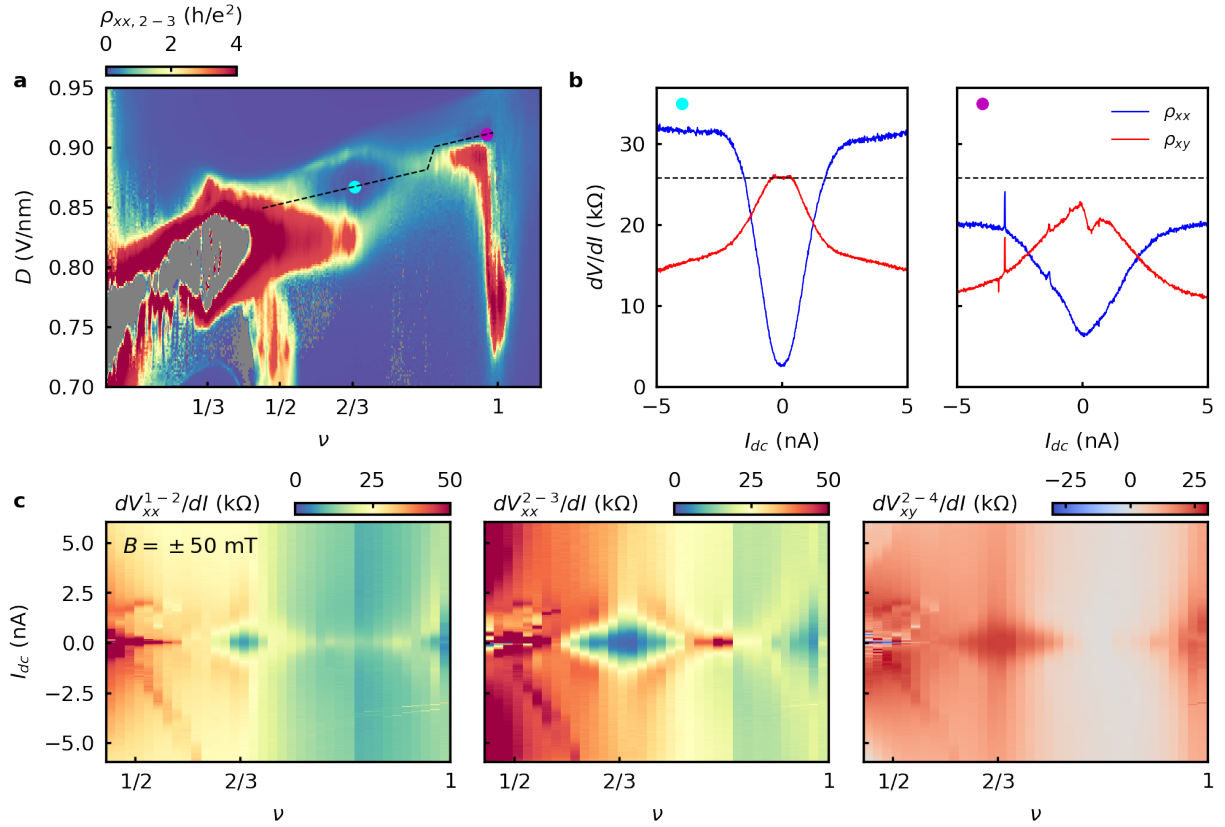


FIG. S6. **Dependence of the TEC states on the bias current.** **a**, Map of ρ_{xx} reproduced from Fig. 1e. The purple and blue circle markers indicate the positions of the measurements in **b**. The black dashed path indicates the path taken for the measurements in **c**. **b**, Differential resistance, dV/dI , measured as a function of I_{dc} with $I_{ac} = 14$ pA at the positions of the blue and purple markers in **a**. At $\nu = 2/3$ (blue circle), ρ_{xy} is very nearly quantized to h/e^2 and ρ_{xx} exhibits a deep minimum only over a very small range of $I_{dc} \lesssim 1$ nA. For larger I_{dc} , ρ_{xy} is rapidly suppressed and ρ_{xx} spikes to a value in excess of h/e^2 . Similar behavior is seen at $\nu = 1$ (purple dot), although the Chern insulator is not as well developed even for vanishing I_{dc} . **c**, Maps of dV/dI as a function of I_{dc} taken along the path of the dashed black path in **a** (anti-) symmetrized at $|B| = \pm 50$ mT. Each panel corresponds to different contact pairs.

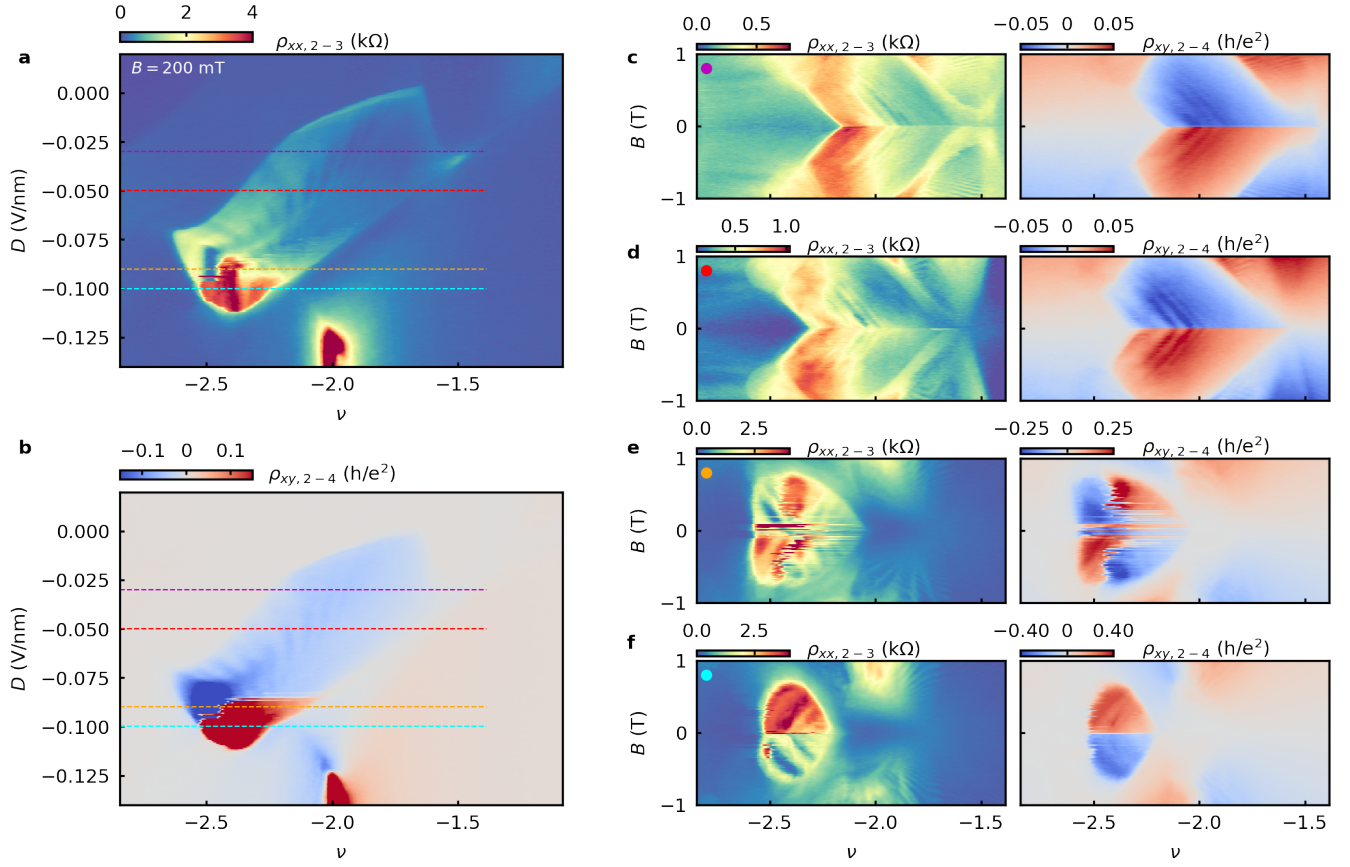


FIG. S7. Landau fans taken at fixed D through the valley-polarized pocket surrounding $\nu = -2$. Maps of **a**, ρ_{xx} , and **b**, ρ_{xy} at $B = +200$ mT, reproduced from Fig. 4a. **c-f**, Landau fans taken at constant D (from top to bottom: -0.03 V/nm, -0.05 V/nm, -0.90 V/nm, -0.10 V/nm). The colored circles correspond to the dashed lines in **a-b**. All data taken with $I_{ac} = 1$ nA.

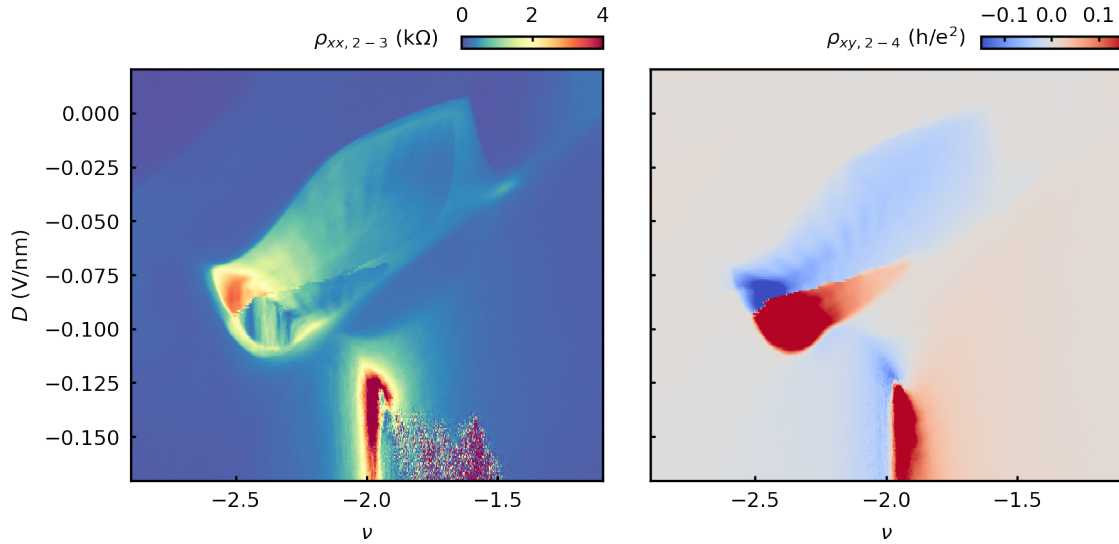


FIG. S8. **Maps of the valley-polarized pocket surrounding $\nu = -2$ taken with lower excitation current.** Similar maps as those shown in Supplementary Information Fig. S7a-b, but with an ac excitation current of 120 pA rather than 1 nA. None of the key features of the maps change as a result of reducing the excitation current (subtle differences between this data and Fig. S7a-b result from sweeping n and D in different directions, which can change the orbital magnetic states, Extended Data Fig. 10d).

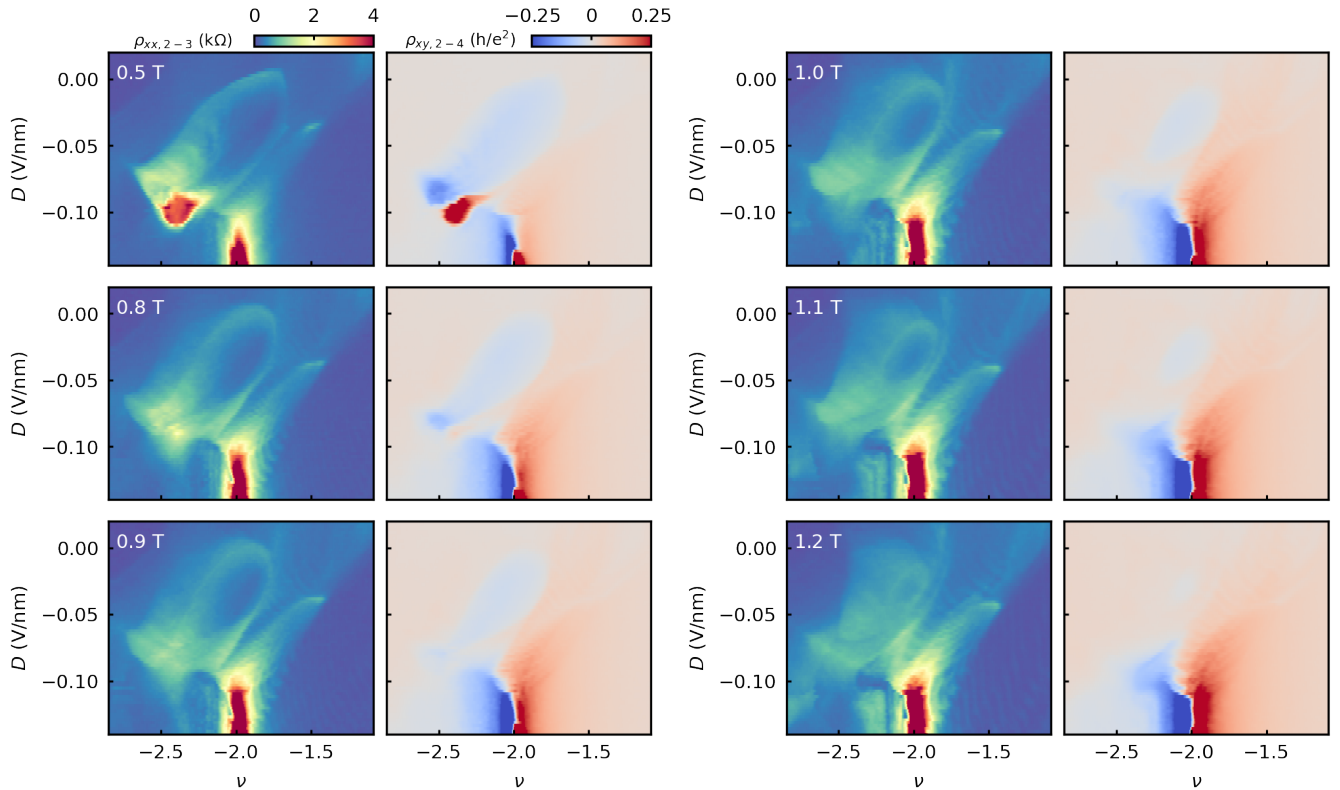


FIG. S9. **Magnetic field-dependence of the valley-polarized pocket surrounding $\nu = -2$.** Maps of ρ_{xx} and ρ_{xy} taken with various values of the magnetic field as denoted in each panel. The valley-polarized pocket appears to be completely quenched at $B = 1.2$ T, consistent with the behavior seen in the Landau fans (e.g., Fig. 4g and Supplementary Information Fig. S7). Data taken with $I_{ac} = 1$ nA. Data is not (anti-)symmetrized.

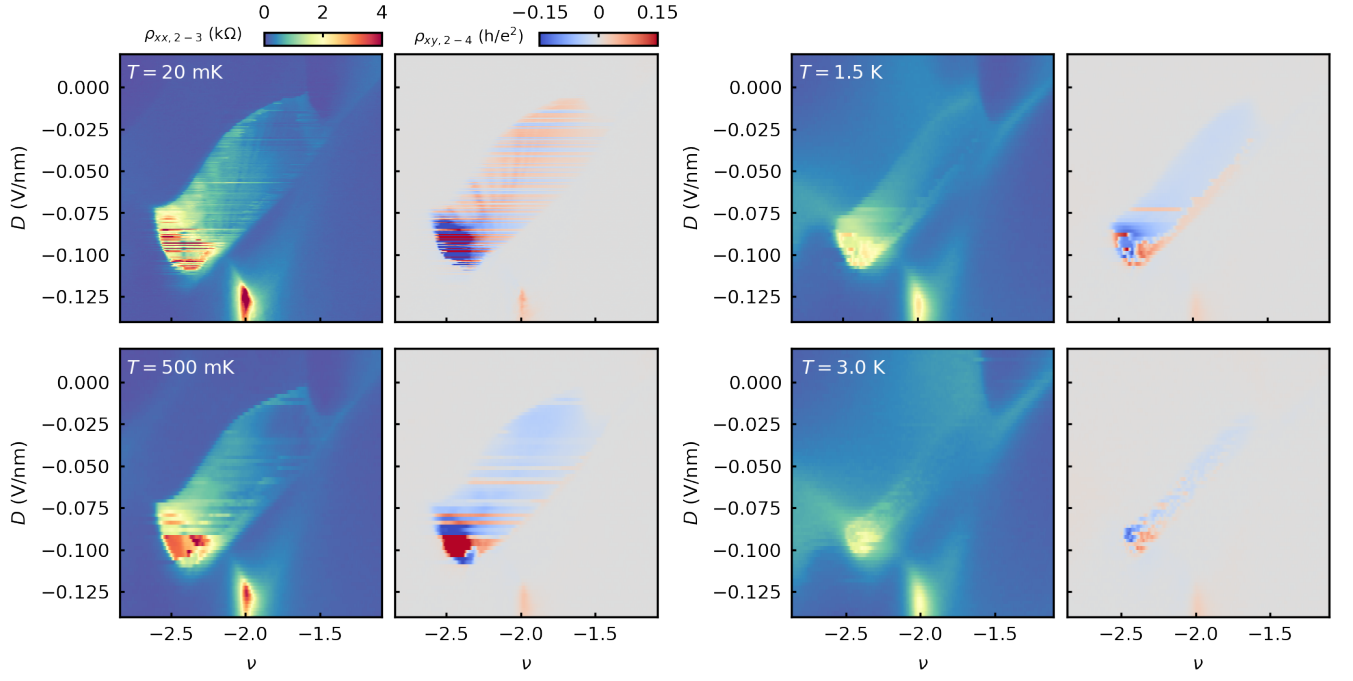


FIG. S10. **Temperature dependence of the valley-polarized pocket surrounding $\nu = -2$.** Maps of ρ_{xx} and ρ_{xy} taken at various temperatures, as denoted in each panel. The valley-polarized pocket is almost completely suppressed at $T = 3$ K. All maps are taken at $B = 0$ and with $I_{ac} = 1$ nA.

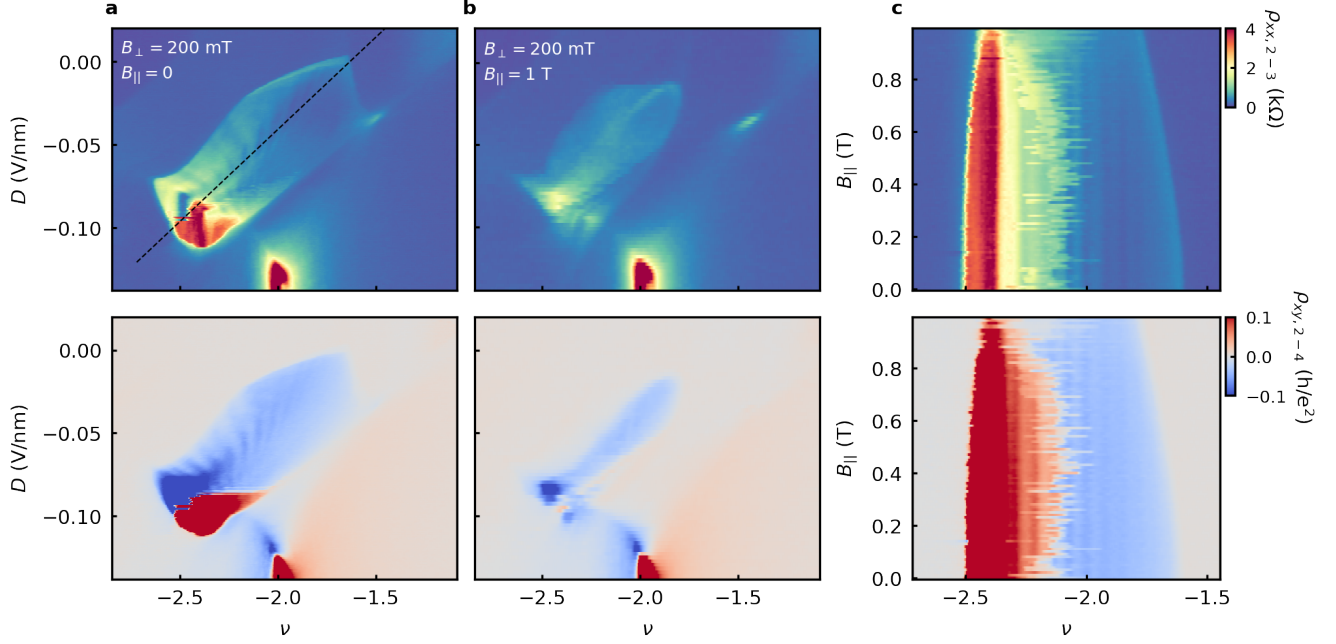


FIG. S11. **In-plane magnetic field dependence of the valley-polarized pocket surrounding $\nu = -2$.** **a**, Maps of ρ_{xx} and ρ_{xy} of the correlated states near $\nu = -2$ taken with an out-of-plane field of $B = 200$ mT (reproduced from Fig. 4a). **b**, The same maps with an additional in-plane magnetic field component, $B_{||} = 1$ T. The extent of the valley-polarized pocket in both n and D is reduced as a result of the in-plane field. **c**, Maps of ρ_{xx} (top) and ρ_{xy} (bottom) taken as a function of $B_{||}$ with a fixed out-of-plane field of $B = 200$ mT. As identified in **b**, the width of the valley-polarized pocket in ν is reduced as $B_{||}$ is raised. The oscillations inside the valley-polarized pocket are pinned to fixed values of ν for all $B_{||}$. Sweeping the doping also induces a flip in the sign of the orbital magnetic state, which also appears to have little dependence on $B_{||}$. Data taken with $I_{ac} = 1$ nA. Data is not (anti-)symmetrized.

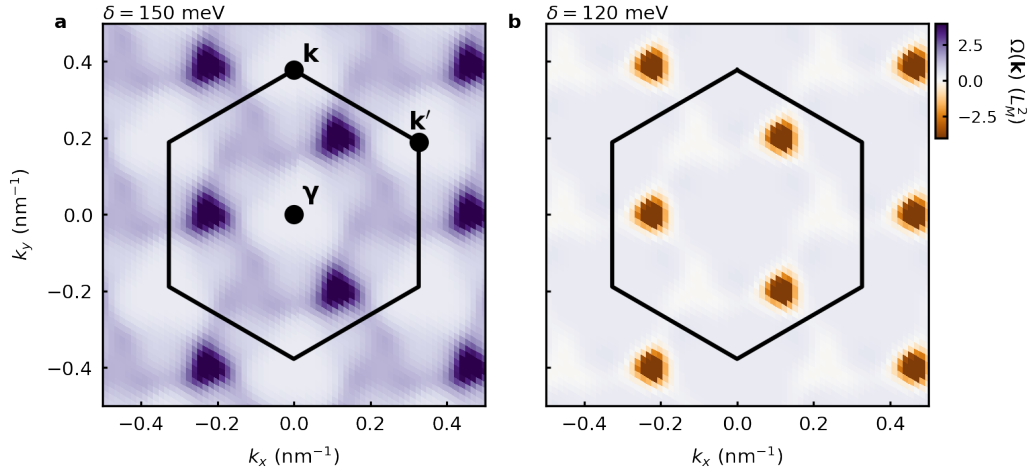


FIG. S12. **Berry curvature distribution of the $\nu = 1$ state from Hartree-Fock.** Berry curvature, $\Omega(\mathbf{k})$, calculated by the Hartree-Fock method at $\nu = 1$ (Fig. 2f) for **a**, $\delta = 150$ meV ($\delta > \delta_c$), and, **b**, $\delta = 120$ meV ($\delta < \delta_c$). The black hexagon shows the moiré Brillouin zone. The integrated Berry curvature over the entire moiré Brillouin zone yields a Chern number of $C = +1$ (0) in **a** (**b**).

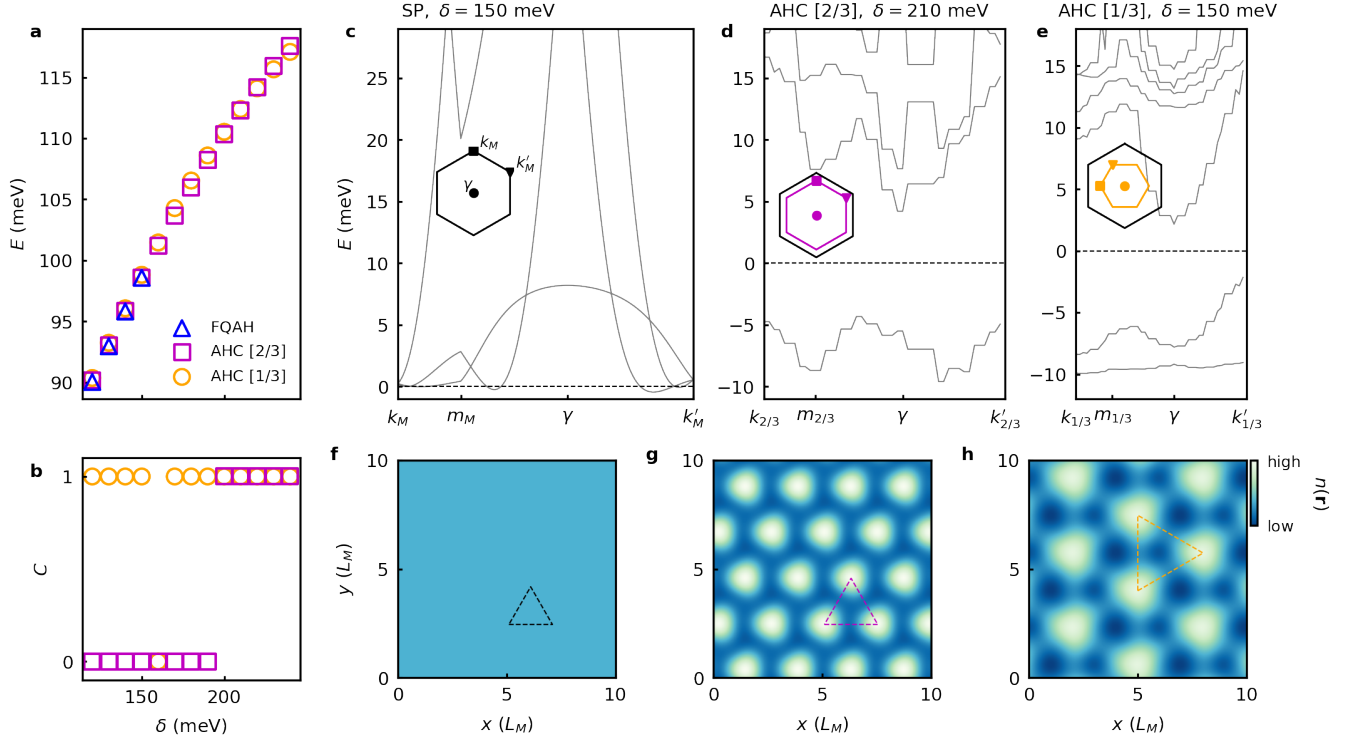


FIG. S13. **Possible ground state orderings at $\nu = 2/3$.** **a**, Energy of the three possible $\nu = 2/3$ ground states as determined by Hartree–Fock calculations in the limit of zero moiré potential as a function of δ (see Methods for details of the calculations): (I) a FQAH state (II) an AHC state with a period of $L_{\text{crystal}} = L_M/\sqrt{2/3}$ (AHC [2/3]), and (III) an AHC state with $L_{\text{crystal}} = L_M/\sqrt{1/3}$ (AHC [1/3]). The energies at each value of δ are very close for each state, within 0.65 meV, rendering a meaningful prediction of the ground state ordering impossible. **b**, Corresponding Chern numbers of the two possible AHC states. **c**, Single particle (SP) band structure calculated with the continuum model at $\delta = 150$ meV (also in the limit of zero moiré potential). The energy axis is taken with respect to the Fermi energy corresponding to $\nu = 2/3$ (dashed black line). The inset shows the moiré Brillouin zone (BZ) with high symmetry points labeled. The subscript M denotes the full moiré BZ. **d**, Hartree–Fock band structure for the AHC [2/3] state with $\delta = 210$ meV. The dashed line is the Fermi energy, which lies within the gap. The inset denotes the original BZ in black and the reduced BZ of the $L_{\text{crystal}} = L_M/\sqrt{2/3}$ state in purple. The same high symmetry points are shown as in **c**, but in the reduced BZ they are denoted by the 2/3 subscripts. **e**, Same as **d**, but for the AHC [1/3] state. Note that the 1/3 BZ (orange) is rotated by 90° for commensuration. **f**, Calculated real space density for the SP band structure in **c**. The density is uniform since the calculation is performed in the limit of zero moiré potential. The black dashed triangle denotes the moiré unit cell. **g**, Real space density for the HF calculation in **d**. The dashed purple triangle corresponds to the unit cell with $L_{\text{crystal}} = L_M/\sqrt{2/3}$. **h**, Real space density for the HF calculation in **e**. The dashed orange triangle corresponds to the unit cell with $L_{\text{crystal}} = L_M/\sqrt{1/3}$. **f–h** are all plotted on the same colorscale.

REFERENCES

- [1] Zhu, J., Li, T., Young, A.F., Shan, J., & Mark, K.F. Quantum oscillations in two-dimensional insulators induced by graphite gates. *Phys. Rev. Lett.* **127**, 247702 (2021).